Long-term monitoring of a dynamically new comet C/2020 V2 (ZTF)

Goldy Ahuja [1,2]★ K. Aravind [1,3] Shashikiran Ganesh [1] Said Hmiddouch,[3,4] Mathieu Vander Donckt,[3] Emmanuel Jehin,[3] Devendra Sahu[5] and T. Sivarani[5]

[1]*Physical Research Laboratory, Ahmedabad, Gujarat-380009, India*
[2]*Indian Institute of Technology Gandhinagar, Palaj, Gujarat-382355, India*
[3]*Space Sciences, Technologies & Astrophysics Research (STAR) Institute, University of Liège, B-4000 Liège, Belgium*
[4]*Cadi Ayyad University (UCA), Oukaimeden Observatory (OUCA), Faculté des Sciences Semlalia (FSSM), High Energy Physics, Astrophysics and Geoscience Laboratory (LPHEAG), Marrakech 40000, Morocco*
[5]*Indian Institute of Astrophysics, Koramangala, Bengaluru, Karnataka – 560034, India*

ABSTRACT

Comet C/2020 V2 (ZTF, Zwicky Transient Facility) is categorized as a dynamically new long-period comet, making its first approach to the inner Solar system. We have observed this comet for around 32 months (from 2022 January to 2024 July) at heliocentric distances from 5.41 au (pre-perihelion) to 5.26 au (post-perihelion) through various telescopes, employing photometric (60 epochs) and spectroscopic techniques (5 epochs). Using these observations, we derived the production rates of different molecules such as $CN(0-0)$, $C_2(\Delta \nu = 0)$, and C_3 and calculated the production rate ratios. The values of the ratios closest to the perihelion are found to be $\log (C_2/CN) = -0.04 \pm 0.03$ and $\log (C_3/CN) = -0.70 \pm 0.04$, which implies a typical carbon composition. The mean photometric broad-band colours are found to be $B - V = 0.77 \pm 0.04$, $V - R = 0.43 \pm 0.04$, $R - I = 0.42 \pm 0.06$, and $B - R = 1.19 \pm 0.04$. The stability of the molecular production rate ratios and mean photometric broad-band colours, pre- and post-perihelion, implies a homogeneous composition. The mean reflectivity gradient for $B - V$ colour is 10.90 ± 3.62 per cent/1000 Å; $V - R$ colour is 6.15 ± 3.51 per cent/1000 Å; and for $R - I$ colour is 4.94 ± 3.56 per cent/1000 Å which is similar to the mean value of the dynamically new comets. Additionally, using an asymmetric non-gravitational force model, we report the comet's nuclear radius to be 1.1 ± 0.1 km. Our results are expected to provide inputs to the selection of a potential dynamically new comet as a target for the *Comet Interceptor* mission.

Key words: techniques: photometric – techniques: image processing – techniques: spectroscopic – comets: general – comets: individual: C/2020 V2.

1 INTRODUCTION

Comets are known as the pristine bodies of the Solar system. They are remnants of the proto-solar nebula, which are distributed in two big reservoirs in the early Solar system. These reservoirs, i.e. the Kuiper Belt and the Oort Cloud, are predicted to be formed due to the giant planetary migration towards the inner Solar system (Gomes et al. 2005; Tsiganis et al. 2005; Morbidelli et al. 2007; Walsh et al. 2011; Brasser & Morbidelli 2013).

Initially, comets are classified based on their orbital period, where short-period comets, hereafter, SPCs, and long-period comets, hereafter, LPCs, are differentiated by whether their orbital period is less than or greater than 200 yr (Levison 1996). The SPCs are further divided into Jupiter-family comets and Halley-type comets, based on the distribution of the comets in the inclination versus eccentricity plot (see fig. 3 in Levison 1996 and fig. 1a in Nesvorný et al. 2017). Jupiter-family comets, hereafter JFCs, show the clump distribution with a median inclination of 12.4° (Brasser & Wang 2015), and

revolve in a prograde orbit for a period of less than 20 yr. Whereas Halley-type comets, hereafter HTCs, have a median inclination of 75° (Wang & Brasser 2014). Several HTCs do have a retrograde orbit (Levison 1992).

Based on numerical simulation by Levison & Duncan (1997), JFCs have been found to be coming from the Kuiper belt. Also, another possibility of the origin of JFCs is from the scattered disc (Duncan & Levison 1997), while the origin of HTCs, due to their varying inclination, is possible from the Oort Cloud (Wang & Brasser 2014; Nesvorný et al. 2017) or from the scattered disc (Levison et al. 2006).

The LPCs are thought to originate from the Oort Cloud (Oort 1950). The LPCs can be further divided based on whether the comet is coming into the inner Solar system for the first time, i.e. a new comet, or it has already visited before, i.e. a returning comet. Those comets whose semimajor axis (i) is more than 10 000 au are called the dynamically new comets, while if the semimajor axis (ii) is less than 10 000 au, they are called returning comets (Levison 1996). Recently, there has been a debate on the limit (check Królikowska & Dybczyński 2010; Dybczyński & Królikowska 2011). Studying dynamically new comets, hereafter DNCs, is essential as they are

★ E-mail: goldy@prl.res.in; goldezz20@gmail.com

coming towards the Sun for the first time, and it is expected that they have never been exposed to the solar radiation after their initial formation and probable migration. The understanding of DNCs is important for the future *Comet Interceptor* mission (Jones et al. 2024), which will be launched to study a least processed object, one that has never been to the inner Solar system since its formation. Therefore, long-term monitoring of these objects is important to understand their evolution as they come to and go beyond perihelion.

Comet C/2020 V2 (ZTF), hereafter V2, was discovered by the Zwicky Transient Facility in 2020 November at a distance of 8.7 au from the Sun. It approached perihelion on 2023 May 08 at a distance of 2.228 au. Comet V2 is a DNC with a semimajor axis of -2321 au at epoch JD2459827.5 and an eccentricity of 1.0009 with a 1σ eccentricity of 2.669×10^{-6} as given in NASA JPL SBDB.[1] It is currently in a hyperbolic orbit. However, just being in a hyperbolic orbit does-not conclude that the comet is a DNC because its orbital parameters can be perturbed due to interaction with giant planets, galactic tidal effects, or non-gravitational forces, which result in changes in its trajectory. Therefore, to predict the orbital parameter of DNC, we need to know its osculating elements in the past at -250 au (negative sign representing that the comet is approaching the Sun) as mentioned in the model by Królikowska & Dybczyński (2010) and Królikowska (2014). Using the CODE (Catalogue of Cometary Orbits and their Dynamical Evolution) catalogue,[2] which is based on Królikowska & Dybczyński (2010), the average $1/a_{\rm orig}$ is 14.88×10^{-6}, which describe this comet as a DNC. Since it is now travelling in a non-periodic orbit, this gives us a unique opportunity to study this body before it leaves the Solar system unless its orbit gets significantly perturbed to a returning trajectory.

In this work, we discuss the results obtained from photometric and spectroscopic observations of comet V2 from the TRAPPIST (Transiting Planets and Planetesimals Small Telescope) telescopes and multiple Indian observatories, respectively. We briefly describe the different telescope facilities used in Section 2 and the data reduction methods for photometry and spectroscopy in Section 3. We mention the data analysis method to calculate the gas production rates and the dust proxy parameter, $Af\rho$ in Sections 4.2 and 4.3. The major spectroscopic and photometric results are discussed in Sections 5 and 5.2. The discussions on both techniques are given in Section 6.

2 OBSERVATIONS

We obtained low-resolution optical spectroscopic and photometric observations using the 2-m Himalayan Chandra Telescope (HCT). We also used the 1.2-m PRL Mount Abu telescope to obtain low-resolution spectra. Additionally, we observed the comet using broad-band photometric observations and comet Hale–Bopp (HB) narrow-band filters (Farnham, Schleicher & A'Hearn 2000) mounted on TRAPPIST.

2.1 Himalayan Chandra Telescope

HCT[3] is a 2-m Ritchey–Chretien, Cassegrain focus, $f/9$ telescope situated at (lat: 32.78 deg N; long 75.96 deg E; alt: 4500 m) the Indian Astronomical Observatory (IAO), in Hanle, India (Prabhu 2014). The

telescope is operated by the Indian Institute of Astrophysics (IIA). The plate scale of the Hanle Faint Object Spectrograph Camera, hereafter HFOSC, instrument is 0.296 arcsec pixel^{-1}. The active area of the CCD is 2048 pixel $\times$ 4096 pixel, which gives the field of view of $\sim$ 10 arcmin $\times$ 20 arcmin. We used HFOSC in both photometric and spectroscopic modes. For spectroscopy, we have taken observations in the CCD dimensions of 1500 pixel $\times$ 3500 pixel to get the spatial coverage of the 11 arcmin across the cometary coma. We used Grism 7, which provides a resolving power ($R = \Delta\lambda/\lambda$) of 1330 and wavelength coverage of 3800–6840 Å. We also used Grism 8 for one observation to increase the spectral range and look for any absorption/emission at a redder wavelength. Grism 8 has a medium resolving power of 2190 with a spectral range of 5800–8350 Å. The comet is observed with a slit having a width of 1.92 arcsec and a length of 11 arcmin, while the standard stars used for flux calibration are observed with a slit of width 15.4 arcsec and a length of 11 arcmin. The slit orientation is in the east–west (E-W) direction. We used the keystone mode mentioned in Aravind et al. (2021) to make sure that the telescope was tracking the comet throughout the exposure. The NASA JPL HORIZONS[4] was used to obtain the comet ephemerides at each epoch. We have taken a separate sky frame after moving the telescope 1° away from the photocentre in the direction of the comet's declination motion. We observed the standard stars BD + 284211 (sdO, Oke 1990) and HD74721 (A0V, Cannon & Pickering 1918; Barnes, Hayes & Observatory 1984) with the wider slit to avoid slit losses. We also observed HD19445, a solar analog (G2V) star, to correct for the comet's continuum. Zero exposure frames were taken to correct the CCD bias, lamp flats to correct the pixel-to-pixel response, and FeNe (iron–neon) and FeAr (iron–argon) lamp spectra for wavelength calibration of the Gr8 and Gr7 spectra, respectively.

For the photometry, we used the CCD with dimensions of 2048 pixel $\times$ 2048 pixel, which provides a field of view of 10 arcmin $\times$ 10 arcmin. We observed the comet with the Bessel *B*, *V*, *R*, and *I* filters. We also observed the Landolt standard field, RU149 (Landolt 1992), at each epoch in all the filters. The bias and twilight flats were obtained regularly. The average seeing in the photometric and spectroscopic observations from HFOSC was 2–2.5 arcsec.

2.2 PRL Mount Abu Observatory

Another spectrograph, the Long slit Intermediate resolution Spectrograph for Astronomy, hereafter LISA, was used at the PRL (Physical Research Laboratory) 1.2-m *f*/13 Mount Abu telescope at Mount Abu (lat: 24.65 N; long: 72.78 E, alt: 1680 m)[5] LISA provides a wavelength coverage of 3800–7000 Å. Venkataramani et al. (2016) and Aravind et al. (2024) have provided further details of this instrument. Since LISA works best on an *f*/5 telescope, we include a focal reducer at the telescopic entrance of the instrument. The plate scale of the instrument is 0.326 arcsec pixel^{-1}. The long slit is 2 arcmin in length and 1.76 arcsec in width, having an orientation in the north–south (N-S) direction. Since we do not have the photometric observation on LISA, we have used the photometric image obtained from HFOSC and added the slits of both LISA and HFOSC instruments as shown in Fig. 1. We collected bias frames, flat frames to correct for the pixel response, and ArNe (argon–neon) lamps to wavelength calibrate the spectra. We observed standard stars HD74721 (A0V) for flux calibration and HD19445 (G2V; Cannon & Pickering 1918) to remove the solar continuum from the comet
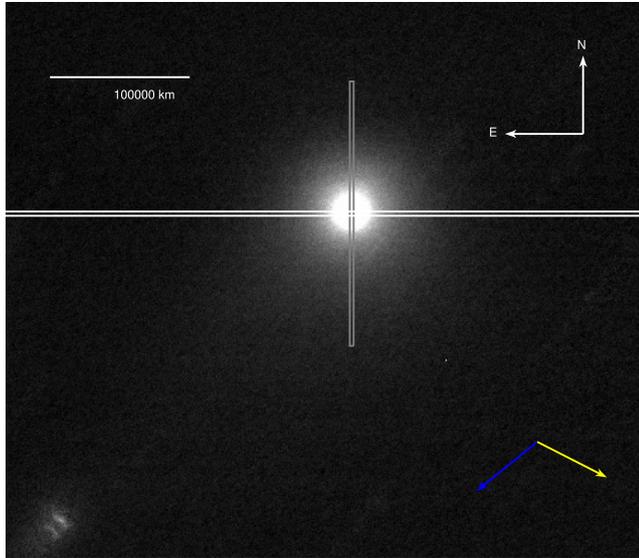

Figure 1. Slits corresponding to HFOSC (white) and LISA (grey) are marked on the comet V2 image observed using HFOSC instrument. The dust-tail orientation and the Sun's direction are marked in blue and yellow.

spectrum. For the LISA observations, the seeing was around 1.8 arcsec. The details of the observations are given in Table 1.

2.3 TRAPPIST

TRAPPIST is a network of two 60-cm robotic telescopes situated in two different hemispheres.[6] TRAPPIST-North (TN) is built at the Oukaimeden Observatory in the Atlas Mountains in Morocco (Barkaoui et al. 2017) while TRAPPIST-South (TS) is located in the Chilean mountains at the La Silla Observatory of ESO (Jehin et al. 2011). These telescopes are remotely controlled. The telescopes are equipped with the cometary HB narrow-band filter set to sample different molecular gaseous emissions such as OH, NH, CN, C_2, and C_3. The telescopes also have dust continuum filters, i.e. BC, GC, and RC for blue, green, and red continuum. The dust-continuum filters are emission-free filters that are used to obtain the proxy dust production parameter and remove the dust contamination from the gas filters. These narrow-band filters were built to observe the emissions only, unlike broad-band filters, which cover a wide range of the spectrum. The details of these filters are mentioned in Farnham et al. (2000). The telescopes also have broad-band Bessel filters, *B*, *V*, *R*, and *I*. TS is equipped with a 2K × 2K FLI Proline CCD with a pixel scale of 0.65 arcsec pixel^{-1}, resulting in a field of view of 22 arcmin × 22 arcmin and TN with an Andor IKONL BEX2 DD (0.59 arcsec pixel^{-1}) with a 20 arcmin × 20 arcmin field of view. The seeing varied between 1.5–3 arcsec during the observations from TRAPPIST telescopes.

3 DATA REDUCTION

In the following section, we discuss the different steps of data reduction performed on the spectrometric data (see Section 3.1) and the photometric data (see Section 3.2).

[6] https://www.trappist.uliege.be/cms/c_5006023/fr/trappist

3.1 Spectroscopic data reduction

Having obtained the spectroscopic data from different telescopes, we now have to obtain the final calibrated frame before carrying out further calculations. The details about the data reduction are explained in the same order as mentioned in Section 2. For instruments like HFOSC on HCT and LISA on Mount Abu Observatory, the data reduction codes have been self-scripted in PYTHON for bias correction and flat-fielding. Since HCT is located at 4500 m, the frames are heavily affected by cosmic rays. We have used the LA COSMIC package developed by Van Dokkum (2001) to remove the cosmic ray contamination.

Using self-scripted PYTHON code, we have extracted a 1D spectrum after removing the background from the standard star, solar analogue star, and comet V2. In the case of a star, we create the background by taking the median values of the counts of at least 50 pixels away from both sides of the photocentre and subtracting it from the star spectrum. In the case of comets, we subtracted the separate sky frame from the comet frame.

After extracting the 1D spectra, different IRAF packages, such as `identify` and `dispcor`, have been used to create the wavelength solution by identifying the lines of the arc lamps. After that, `standard` and `sensfunc` have been employed to make the sensitivity function. Finally, the CALIBRATE package has been applied to obtain the flux-calibrated data.

The final step is to remove the solar continuum spectrum from the comet's spectrum. For this, we use the method explained in Ivanova et al. (2021). The first step is to normalize the flux-calibrated comet's spectrum with the spectrum of the solar analogue star. Then, to correct for the reddening, we use the continuum windows mentioned in Ivanova et al. (2021) to make the comet and solar polynomials, then take the ratio of these two polynomials and multiply with the solar spectrum to get the synthetic dust spectrum. Finally, we subtract this spectrum from the comet spectrum to get the continuum-corrected, flux-calibrated comet spectrum.

This is the general method followed for reducing the 2D raw data to get the final 1D spectrum to be used for analysis. However, if the slit is not wide enough, then other factors also need to be considered, such as the slit correction and the atmospheric dispersion correction, which will be discussed in the following subsections.

3.1.1 Slit correction

As we have mentioned in Section 2.2, the LISA slit size is 1.76 arcsec; therefore, in conditions of bad seeing, the complete flux of a standard star will not enter the slit, affecting the sensitivity function of the instrument. This results in the overestimation of the object's absolute flux. Hence, to correct for it, we must multiply our object's flux-calibrated spectrum by the slit-correction factor. The slit correction factor is based on calculating the FWHM (full width half-maximum) by fitting a Gaussian profile along a spatial axis. It is then used to calculate the error function. This function varies with wavelength. The complete details are given by Lee & Park (2006). This correction factor was not required while reducing the HCT data because the slit used to observe the standard star was wide enough (15.4 arcsec).

3.1.2 Atmospheric dispersion correction

We also need to correct LISA spectra for the atmospheric dispersion, which depends on the star's airmass, the dry pressure at the observatory elevation (in mm hg), the water vapour pressure (in mm hg),

Table 1. Details of observations from Indian telescopes.

Date	DTP[a] (d)	r[b] (au)	Δ[c] (au)	Time (UT)	Telescope facility	Instrument	Observation type	Phase angle (°)	Airmass
2022 Oct 04	−215	−3.27	3.58	22:40	HCT	HFOSC	Imaging (R), Spectroscopy (Gr7)	15.96	1.96
2022 Nov 22	−166	−2.91	2.54	20:16	HCT	HFOSC	Imaging (B, V, R), Spectroscopy (Gr7, Gr8)	19.38	1.81
2022 Dec 16	−142	−2.75	2.17	14:59	HCT	HFOSC	Imaging (B, V, R), Spectroscopy (Gr7)	18.70	1.99
2022 Dec 22	−136	−2.72	2.12	18:08	PRL	LISA	Spectroscopy	18.76	2.10
2023 Sept 21	136	2.71	1.86	20:10	HCT	HFOSC	Spectroscopy (Gr7)	13.68	1.93

Notes. [a] Days to perihelion.
[b] Heliocentric distance.
[c] Geocentric distance.

and the temperature (in Celsius). The dispersion causes the star's light at different wavelengths to get shifted by some arcseconds with respect to the central wavelength at 5000 Å, which is responsible for the low photon counts at the bluer and redder sides of this central wavelength. The detailed methods are given in Filippenko (1982) and Stone (1996).

3.2 Photometric data reduction

The photometric data sets come from two telescopes, HCT and TRAPPIST. We describe the data reduction of the two different telescopes below.

3.2.1 HFOSC photometric data reduction

To reduce the images observed from HFOSC, we used self-scripted PYTHON codes to create the master-bias and master-flat files. We then subtracted the master bias and divided the master flat files from all the comet and field star frames. The PHOTUTILS module from the ASTROPY package (Astropy Collaboration 2013) was used to calibrate the standard star frames. We took the extinction coefficients from Stalin et al. (2008) for the location of HCT. The apertures, which were 2–3 × FWHM, were used to measure the magnitudes of the standard field stars and calculate the zero-point. The computed zero-point is further used to obtain the magnitude of the comet for an aperture size of 5 arcsec.

3.2.2 TRAPPIST photometric data reduction

Comet V2 was observed using both narrow-band and broad-band filters with the TN and TS telescopes (Jehin et al. 2011). The observation campaign was conducted from 2022 January 11 ($r = 5.41$ au, pre-perihelion) to 2024 August 13 ($r = 5.26$ au, post-perihelion), covering the comet's evolution over 32 months around perihelion to analyse long-term variations in the gas and dust activity. For data reduction, we applied standard procedures, including bias, dark, and flat-field corrections, followed by sky contamination removal and flux calibration using standard stars. Absolute flux calibration was performed when conditions were photometric by observing standard stars defined for the Comet HB narrow-band filter set (Farnham et al. 2000).

4 DATA ANALYSIS

In this section, we have used the continuum-corrected spectrum to calculate the gas production rates of different molecules such as CN, C_2, and C_3 using Haser (1957) modelling (details provided in Sections 4.1 and 4.2) and the dust proxy parameter $Af\rho$ (details provided in Section 4.3).

4.1 Column density profile

After obtaining the final reduced (wavelength-calibrated, flux-calibrated, and continuum-corrected) spectra, we calculated the column density along the slit direction (y) using the method in section 5 of the paper by Langland-Shula & Smith (2011).

$$N(y) = \frac{4\pi}{g} \frac{F(y)}{\Omega}. \tag{1}$$

Here, g is the fluorescence efficiency of the molecules, and Ω is the solid angle defined by the multiplication of the slit width and pixels extracted in the spatial axis (p). To find p, we measured the half width at half-maxima of the standard star along the spatial direction and used it to bin the pixels. F is the integrated flux along the slit direction of different molecules integrated at the wavelength range mentioned in table 5 of Langland-Shula & Smith (2011). The values of g for different molecules are given in table 6 of Langland-Shula & Smith (2011). The fluorescence efficiency factor has an inverse relationship with the heliocentric distance ($g \propto r_h^{-n}$). In the case of CN, due to the Swings (1941) effect, the fluorescence efficiency depends on the comet's velocity with respect to the Sun. Based on the Swings effect, Schleicher (2010) has given the method to calculate the g-factor using the double interpolation of the heliocentric distance and velocity. Using the values of different parameters, we calculate the column density from equation (1).

4.2 Haser model

The observed column density described in Section 4.1 is then compared with the theoretical column density generated using Haser's model given by Haser (1957).

Haser's model is a simple two-component model in which gas is assumed to sublimate in a spherically symmetric way at a constant velocity from the nucleus of radius R. It considers that the daughter molecules come out as the only product of the parent molecules. The number density of daughter molecules in the coma is given by:

$$n(R) = \frac{Q}{4\pi v_{\text{flow}} R^2} \frac{\beta_0}{\beta_0 - \beta_1} \left(e^{-\beta_1 R} - e^{-\beta_0 R} \right) \tag{2}$$

where β_0 and β_1 are the inverse scale lengths of the parent and daughter molecules. We have used the scale lengths given by A'Hearn et al. (1995). v_{flow} is the outflow velocity of the daughter molecules, which has been considered to be 1 km s^{-1} and Q is the production rate of the daughter molecules.

The density will be integrated along the line-of-sight distance z, which is related to the nucleus size R and slit aperture y along the spatial axis. It is given by $R^2 = y^2 + z^2$, if the comet is placed at the

centre of the slit $x = 0$. Therefore, we get:

$$N(y) = \int_{-\infty}^{\infty} (n(R)) \, dz \tag{3}$$

On integrating it, we get:

$$N(y) = \frac{Q}{2\pi v_{\text{flow}}} \frac{\beta_0}{\beta_0 - \beta_1} \int_0^{\infty} \left(e^{-\beta_1 R} - e^{-\beta_0 R} \right) dz \tag{4}$$

The chi-square minimization between the observed column density and the theoretical column density was used to obtain the production rates of different molecules. For TRAPPIST, the emission from the gaseous species OH, CN, C_3, and C_2 were measured using HB narrow-band filters, and their production rates were calculated using the Haser model. The model fitting was performed at a projected distance of 10 000 km from the nucleus. Similarly, for the long-slit spectra, the HB filter passband for CN, C_3, and C_2 were used to calculate the production rates of these molecules from 10 000 km onwards.

When the molecular emission is not strong in the comet spectrum, there is difficulty in removing the continuum, which could add a significant error in the computation of the column density profile, like for this comet. Therefore, we have also used another method described by Aravind et al. (2021) and Langland-Shula & Smith (2011). The method allows us to calculate the number of molecules for a given aperture using the relation given below:

$$N = \frac{4\pi \Delta^2}{g} \times F \tag{5}$$

Here, g is the fluorescence efficiency for different molecules, Δ is the geocentric distance, and F is the flux calculated for different molecules in an aperture. The number of molecules is then extrapolated to mimic the number of molecules in the cometary coma using the Haser Fraction (Fink Uwe & Hicks 1996) given by Schleicher.[7] The total number of molecules is divided by the respective molecular lifetime given in A'Hearn et al. (1995) to get the production rate of different molecules.

4.3 Dust proxy parameter – $Af\rho$

The next important parameter in the case of comets is to know the dust activity in the cometary coma. It also helps to calculate the dust-to-gas ratio, a parameter to decide whether the comet is dust- or gas-rich. A'Hearn et al. (1984) have introduced a parameter $Af\rho$, which is a proxy of the dust production rate in comets. $Af\rho$ is a product of the bond Albedo (A), the filling factor of grains in our field of view (f), and the aperture radius ρ. Filling factor, f is given by:

$$f = \frac{N(\rho)\sigma}{\pi \rho^2} \tag{6}$$

where $N(\rho)$ is the number of grains present in a circular aperture of radius ρ, σ is the area of a single grain, and A is a dimensionless quantity that depends on the scattering or phase angle θ. As $N(\rho)$ is a dimensionless quantity, σ has dimension of cm^2 and ρ has a dimension of cm, f becomes a dimensionless quantity which makes $Af\rho$ depend only on the dimension of ρ i.e. in cm.

A'Hearn et al. (1984) have given the details to calculate this parameter. They have defined the total luminosity of a comet as:

$$L = AN(\rho)\sigma \frac{F_{\odot}}{r^2} \tag{7}$$

[7] https://asteroid.lowell.edu/comet/haser

where A, σ are defined earlier, $F_{\odot}$ is the solar flux at 1 au, and r is the heliocentric distance, given in au. Using the definition of filling factor given by equation (6), we can get:

$$L = Af\pi\rho^2 \frac{F_{\odot}}{r^2} \tag{8}$$

Also, the luminosity of the comet can be defined as:

$$L = 4\pi\Delta^2 F_{\text{com}} \tag{9}$$

where F_{com} is the flux of a comet within the continuum region, i.e. BC, GC, and RC, defined by Farnham et al. (2000). From equations (9) and (8), we can get:

$$Af = \frac{(2\Delta r)^2}{\rho^2} \frac{F_{\text{com}}}{F_{\odot}} \tag{10}$$

or, the dust proxy parameter $Af\rho$ is,

$$Af\rho = \frac{(2\Delta r)^2}{\rho^2} \frac{F_{\text{com}}}{F_{\odot}} \rho \tag{11}$$

For narrow-band photometry, the $Af\rho$ parameter was derived from the dust continuum profiles using HB cometary dust filters BC, GC, and RC. The phase angle correction to $0°$ was applied using the details mentioned in Schleicher (2007) to obtain $A(0)f\rho$. The main uncertainties in production rates and $Af\rho$ stem from absolute flux calibration and sky background subtraction. An uncertainty of 5 per cent was considered for extinction coefficients, which is negligible at low airmass but becomes significant at high airmass. Sky background uncertainty was estimated at the 3σ level and incorporated into the final uncertainties on production rates. The total errors reported in the following sections are a quadratic combination of sky background and extinction coefficient uncertainties.

For long-slit spectroscopy, we have summed three to five pixels along the spatial axis based on seeing. We used the geometric correction factor given by Langland-Shula & Smith (2011) to convert the long slit into a circular aperture. The full disc flux in different continuum bands, such as BC and GC, is convolved with the filter profile of these bands. Using equation (11), we get the value of $Af\rho$ at a particular phase angle value, θ. and normalized to $0°$. It is done by dividing the value of $Af\rho$ by the phase function $S(\theta)$ given by Schleicher, Millis & Birch (1998). We have used the online phase function table on the Schleicher website.[8]

5 RESULTS

The results obtained using the spectroscopic and photometric observations are given below.

5.1 Spectroscopic results

We have taken spectroscopic observations at six different epochs (ref: Table 1), four from the HFOSC instrument on the 2 m HCT and two from the LISA instrument mounted on the PRL 1.2 m telescope. The details of the HFOSC and LISA instruments are mentioned in Sections 2.1 and 2.2. Out of the six spectra, five spectra are observed pre-perihelion, and one spectrum is taken post-perihelion.

We have reduced the low-resolution spectroscopic data sets using the methods given in Section 3.1 and calculated the production rates of different molecules such as CN $(0 - 0)$, $C_2(\Delta = 0)$, and $C_3(0 - 0)$. The prominent molecular emission bands are marked in Fig. 2. The details of the production rates are given in Table 2.

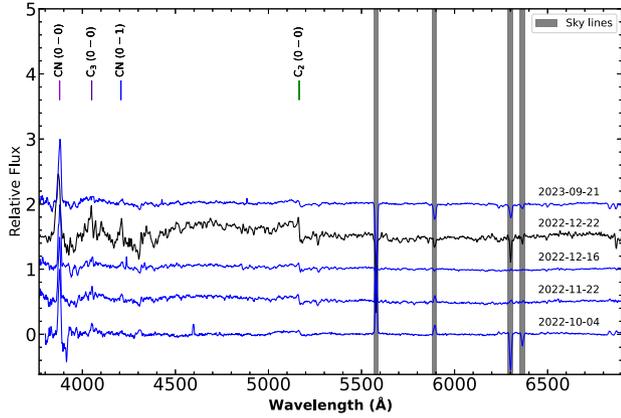[8] https://asteroid.lowell.edu/comet/dustphase/table

Figure 2. Spectra of comet V2 (ZTF) observed from HFOSC/HCT (in blue) and LISA/PRL (in black). The second-from-top spectrum was obtained with LISA/PRL, and the remaining four spectra were obtained with HFOSC/HCT. Prominent emission bands are marked, and the skylines are masked. The spectrum is normalized and spaced by 0.5 relative flux units for clarity.

5.2 Photometric results

In Table 3, we mention the molecular gas production rates like CN(0 − 0) at 3880 Å, $C_2(\Delta\nu = 0)$ at 5165Å, C_3(0–0) at 4050 Å, and OH (0 − 0) at 3097 Å. The images through the CN, C_2, and C_3 gas filters are shown in Appendix B (Figs B1a, B2a, and B3a). These molecular production rates were calculated using observations from the TN. We have also derived the dust proxy parameter ($Af\rho$) defined in Section 4.3. The variation of production rates of different molecules are shown in Appendix A (Figs A1a–d) and the variation of the dust proxy parameter are plotted in Appendix A (Figs A1e–h).

Table C1 presents the apparent photometric magnitudes of comet V2 in broad-band filters, i.e. *B*, *V*, *R*, and *I*, from TN and TS telescopes, and Table 3 mentions the magnitude in broad-band *B*, *V*, and *R* filters observed from HCT. We have plotted the light curves in *B*, *V*, *R*, and *I* filters comprising both HCT and TRAPPIST telescopes in Fig. 3. The dash–dotted curve represents the variation of phase angle (Sun–Comet–Observer angle) with heliocentric distance. The low phase angles close to perihelion (Fig. 3) show that the comet was behind the Sun, as seen from the Earth, and hence it was not conducive for observations.

6 DISCUSSION

6.1 Production rates and rate ratios

The molecular production rates and the rate ratios for the spectroscopic and photometric measurements are given in Tables 2 and 3, respectively. The variation of the production rates of OH, CN, C_2, and C_3 molecules with respect to heliocentric distance (in au) and

days to perihelion (DTP, in days) are given in Figs A1(a)–(d). The computed gas production rates and the rate ratios can provide hints of the chemical composition of a comet. The intensity ratios of C_2 to CN are directly correlated to the aromatic rings, as mentioned by Portnov, Rosenwaks & Bar (2003) and Mousavi et al. (2015) using laser-induced breakdown spectroscopy. A'Hearn et al. (1995) have provided the limits of the production rate ratios, such as C_2/CN and C_3/CN, to understand whether the comet has a carbon-typical composition or a carbon-depleted composition.

In Figs 4 and 5, we have plotted the production rate ratios, C_2/CN and C_3/CN, as a function of the DTP in days and the heliocentric distance in au. We have shown two regions: one in blue, which represents the range for typical carbon composition of the comets, and the second in orange, which represents the depleted composition of comets. The centre line of every region represents the respective median value. The observations from the LISA instrument are shown as a black triangle, from HFOSC are shown as a star, and from TRAPPIST are marked as a red square. The vertical dotted line represents the perihelion distance, which is 2.23 au. Fig. 4 shows a slight variation in the production rate ratio C_2/CN with the heliocentric distance. We see the comet appears to become carbon-depleted at a distance larger than about 2.5 au, which could be due to the drop in the production of C_2 molecules. However, in Fig. 5, the production rate ratio C_3/CN is consistently typical over a large range in heliocentric distance. Therefore, we believe that comet V2 has a typical carbon chemical composition. In addition, we have plotted the dust-to-gas ratio, which is defined as the ratio of the dust proxy parameter $Af\rho$ in the BC filter to the production rate of the CN molecule. As shown in Fig. 6, the comet has a dust-rich composition.

We have also fitted a power-law function to the variation of the production rates of different molecules, such as OH, CN, C_2, C_3, and pre- and post-perihelion. The computed power-law slopes are given in Table 4. We could not calculate the power-law slopes for OH and C_3 due to insufficient points post-perihelion. The slope of C_2 post-perihelion is seemingly higher due to the sharp drop in C_2 production beyond 2.5 au. This is why the production rate ratio for C_2/CN should be looked at under 2.5 au to determine the carbon-depleted/typical nature of the comet, as also mentioned in Opitom et al. (2015).

6.2 Photometric colours

Using the values in Table C1, we have calculated different colours such as $B - V$, $V - R$, $R - I$, and $B - R$. The mean values of these colours are $B - V = 0.77 \pm 0.04$, $V - R = 0.43 \pm 0.04$, $R - I = 0.42 \pm 0.06$, and $B - R = 1.19 \pm 0.04$. We have compared these colours with the known median colours of active LPCs, calculated by Jewitt (2015), which are $B - V = 0.78 \pm 0.02$, $V - R = 0.47 \pm 0.02$, $R - I = 0.42 \pm 0.03$, $B - R = 1.24 \pm 0.02$. Since this comet is

Table 2. Spectroscopic molecular gas production rates, $Af\rho$ in BC and GC are calculated using observations from HFOSC/HCT and LISA/PRL. Broad-band photometric calculations are done using observations from HFOSC/HCT.

Date	DTP (d)	*r* (au)	Δ (au)	Production rates ($\times 10^{25}$ molecules s^{-1})			$A(\theta = 0°)f\rho$ ($\times 10^3$ cm)		Magnitudes (dimensionless)		
				Q(CN)	*Q*(C$_2$)	*Q*(C$_3$)	BC	GC	*B*	*V*	*R*
2022 Oct 04	−215	−3.27	3.58	14.7 ± 1.0	6.9 ± 1.2	2.1 ± 1.3	4748 ± 2128	6623 ± 1703	–	–	13.56 ± 0.09
2022 Nov 22	−166	−2.91	2.54	19.3 ± 1.3	13.8 ± 3.9	5.1 ± 2.2	11 274 ± 552	12 192 ± 393	14.47 ± 0.10	13.45 ± 0.10	12.93 ± 0.10
2022 Dec 16	−142	−2.75	2.17	18.9 ± 1.0	13.9 ± 1.7	2.3 ± 1.0	9539 ± 364	11 529 ± 268	13.89 ± 0.06	12.93 ± 0.10	12.43 ± 0.10
2022 Dec 22	−136	−2.71	2.12	18.0 ± 0.9	13.8 ± 2.9	2.5 ± 0.6	9108 ± 561	7277 ± 561	–	–	–
2023 Sept 21	136	2.71	1.86	7.4 ± 0.4	4.9 ± 1.5	2.0 ± 0.7	3884 ± 230	4752 ± 153	–	–	–

Table 3. TRAPPIST photometric gas production rates and $Af\rho$ in BC, GC, and RC, observed from TN observatory.

Date	DTP (d)	r (au)	Δ (au)	Production rates (× 10^{25} molecules s^{-1}) Q(CN)	Q(C$_2$)	Q(C$_3$)	Q(OH) × 10^3	$A(\theta = 0°)f\rho$ (cm) BC	GC	RC
2022 Nov 04	−184	−3.04	2.91	11.3 ± 0.6	6.8 ± 0.5	–	0.7 ± 0.4	8644 ± 164	–	9561 ± 43
2022 Nov 11	−177	−2.99	2.76	11.2 ± 0.6	7.8 ± 0.7	1.8 ± 0.3	0.5 ± 0.6	7846 ± 201	–	9533 ± 115
2022 Nov 15	−173	−2.96	2.67	12.3 ± 0.6	9.7 ± 0.8	2.9 ± 0.2	1.0 ± 0.7	8155 ± 166	–	9525 ± 59
2022 Nov 22	−166	−2.91	2.53	12.8 ± 0.6	9.3 ± 0.8	2.4 ± 0.2	1.3 ± 0.4	8780 ± 158	–	9783 ± 50
2022 Nov 28	−160	−2.87	2.42	12.5 ± 0.6	9.8 ± 0.8	2.9 ± 0.2	1.0 ± 0.5	8360 ± 153	–	9940 ± 47
2022 Nov 29	−159	−2.86	2.41	12.9 ± 0.6	8.1 ± 0.6	2.2 ± 0.2	1.0 ± 0.4	8585 ± 158	–	10 674 ± 41
2022 Dec 15	−143	−2.76	2.18	16.0 ± 0.9	10.3 ± 1.0	3.6 ± 0.3	–	7834 ± 164	–	9090 ± 67
2022 Dec 16	−142	−2.75	2.17	15.7 ± 0.9	–	–	2.0 ± 0.7	9117 ± 192	–	–
2022 Dec 23	−136	−2.71	2.11	16.2 ± 0.8	11.8 ± 1.0	2.7 ± 0.3	2.4 ± 0.8	8635 ± 183	9224 ± 116	10 435 ± 54
2022 Dec 27	−132	−2.68	2.08	17.4 ± 1.0	14.7 ± 0.9	3.9 ± 0.3	2.1 ± 0.7	8789 ± 179	9190 ± 108	10 900 ± 60
2023 Jan 09	−119	−2.60	2.07	18.0 ± 0.8	17.8 ± 1.1	3.9 ± 0.3	3.4 ± 0.8	8713 ± 166	9200 ± 126	10 543 ± 103
2023 Jan 14	−114	−2.58	2.08	18.4 ± 0.8	15.7 ± 1.1	4.3 ± 0.3	4.2 ± 1.0	8257 ± 180	8724 ± 113	10 318 ± 100
2023 Jan 19	−109	−2.55	2.11	20.0 ± 0.8	16.1 ± 1.0	3.7 ± 0.3	4.2 ± 0.8	8504 ± 187	–	10 494 ± 153
2023 Mar 03	−66	−2.35	2.65	18.0 ± 0.7	17.0 ± 1.0	3.8 ± 0.3	6.9 ± 1.4	7246 ± 219	7475 ± 146	8927 ± 82
2023 Aug 18	103	2.52	2.08	8.8 ± 0.3	11.6 ± 0.7	–	–	3616 ± 61	–	5520 ±33
2023 Aug 29	114	2.58	1.95	8.6 ± 0.4	10.0 ± 0.6	1.6 ± 0.2	–	4905 ± 120	5355 ± 71	6097 ± 36
2023 Sept 19	134	2.70	1.86	8.2 ± 0.5	6.8 ± 0.8	–	0.3 ± 0.4	6258 ± 57	–	–
2023 Sept 23	138	2.72	1.87	7.3 ± 0.5	7.6 ± 0.8	–	0.3 ± 0.5	5615 ± 151	–	6630 ± 50
2023 Oct 07	152	2.81	1.99	6.2 ± 0.6	4.0 ± 0.7	–	–	5902 ± 176	–	6553 ± 48
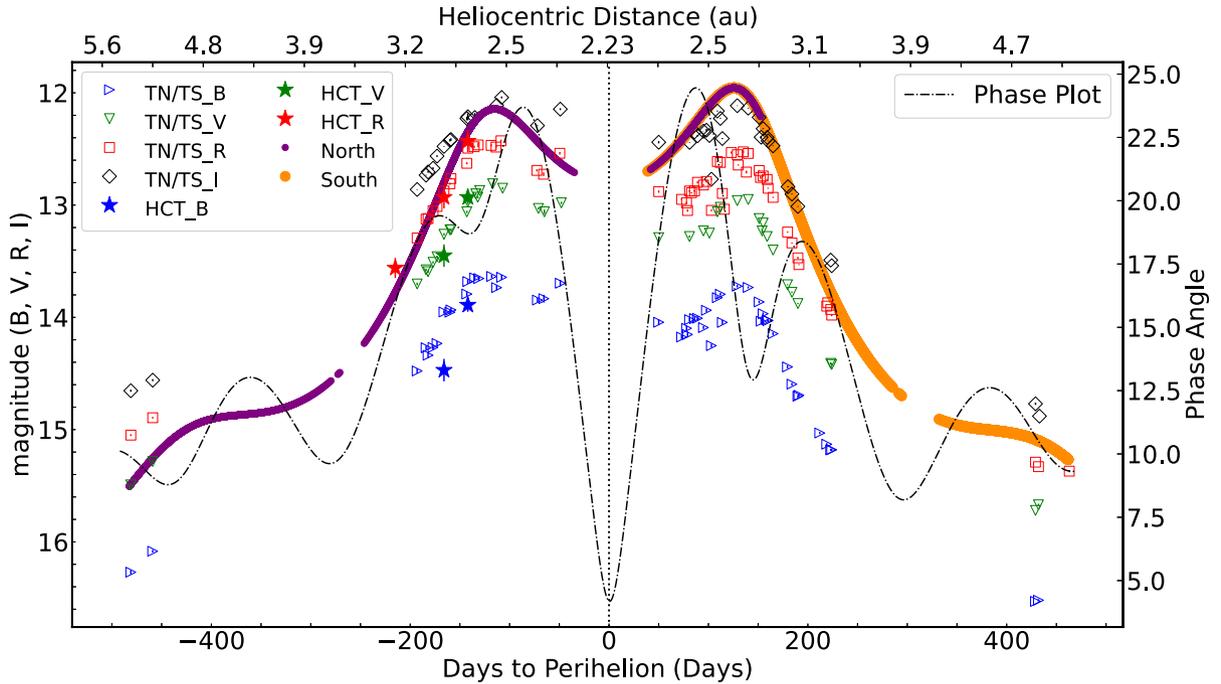
Figure 3. Light curve of comet V2 in *B* (in blue), *V* (in green), *R* (in red), and *I* (in black) filters from the HCT and TRAPPIST. The availability of the comet for observations from the HCT and TN is shown as purple dots (labelled North). Similarly, orange dots are used for the TS (labelled South). They are marked as per the expected magnitude given by NASA JPL HORIZONS. The vertical dotted line, marked in this figure (and all others), represents the perihelion distance, which is 2.23 au. The dash–dotted line represents the variation of the phase angle (Sun–Comet–Earth angle) with heliocentric distance.

a DNC, we also compared its colours with Kulyk et al. (2018), which has shown that the median $B − V$ and $V − I$ colours for DNCs are 0.80 ± 0.07 and 0.44 ± 0.07. We have made the colour–colour plot of the $B − V$ and $V − R$ colours of different DNCs along with comet V2, as shown in Fig. 7 and found that comet V2's mean colours are in close agreement with many reported DNCs. In Figs 8 and 9, we have marked the 1σ range of DNCs with blue and the 1σ range of LPCs with orange. As shown in the figures, there is a significant variation in the different colours of the comet, which could be due

to the varying activity of comet V2, as also mentioned in Voitko & Ivanova (2024).

The mean $B − V$ pre-perihelion colour is 0.76 ± 0.04 and post-perihelion is 0.78 ± 0.04. Similarly, the mean value of $V − R$ pre-perihelion is 0.43 ± 0.04 and post-perihelion is 0.43 ± 0.04. For $R − I$, mean pre-perihelion colour is 0.38 ± 0.05 and post-perihelion is 0.43 ± 0.05. For $B − R$, the mean value for pre-perihelion is 1.18 ± 0.04 and for post-perihelion is 1.21 ± 0.04. As can be seen, the mean colours of the comet during pre- and post-perihelion have not
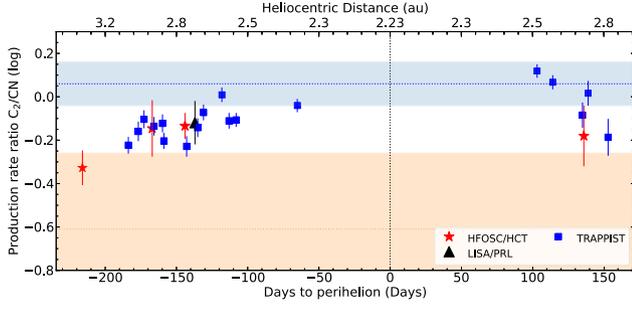
Figure 4. Variation of C_2/CN with the heliocentric distance. We have marked the 1σ range of the typical region with blue and the 1σ range of the depleted region with orange. The observation from TRAPPIST is marked as blue square, the observation from HFOSC/HCT is marked as red star, and the observation from LISA/PRL is marked as black triangle.
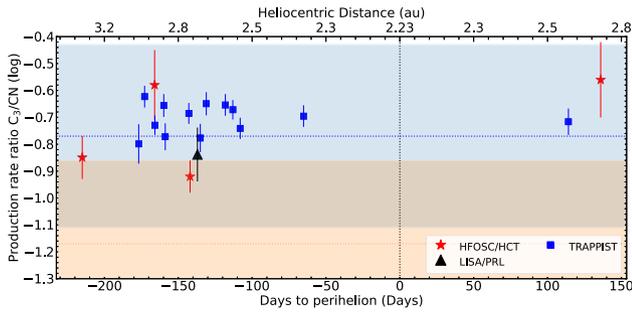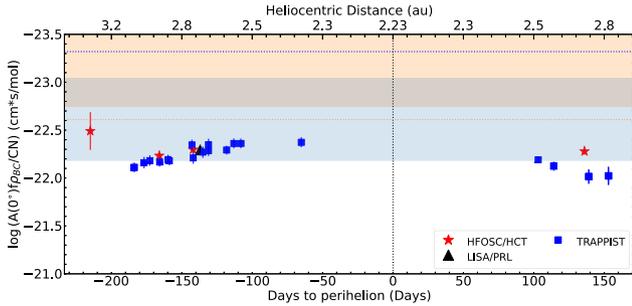

Figure 5. Variation of C_3/CN with the heliocentric distance. We have marked the 1σ range of the typical region with blue and the 1σ range of the depleted region with orange.

Figure 6. Variation of $Af\rho_{BC}$/CN with the heliocentric distance. We have marked the 1σ range of dust-rich with blue and the 1σ range of dust-poor with orange.

Table 4. Computed power-law slopes for different molecules, i.e. OH, CN, C_2, and C_3 at pre- and post-perihelion.

Species	r-dependence	
	Pre-perihelion	Post-perihelion
OH	-10.07 ± 0.75	–
CN	-1.84 ± 0.49	-3.56 ± 1.65
C_2	-3.65 ± 0.52	-9.13 ± 2.00
C_3	-3.51 ± 1.50	–
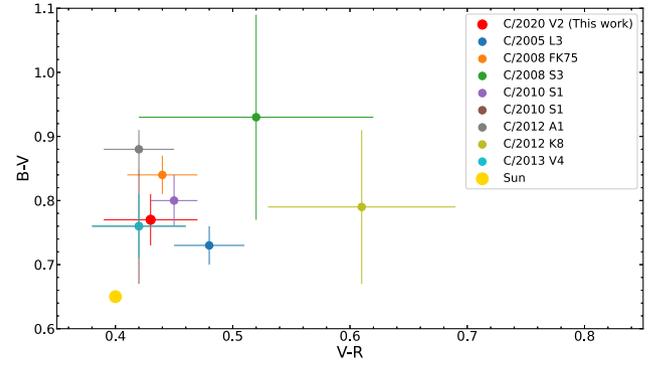
Figure 7. Colour–colour plot of $B - V$ versus $V - R$ of different DNCs (data are taken from Kulyk et al. 2018). The solar colour is marked as yellow and median colour of comet V2 is marked as red.
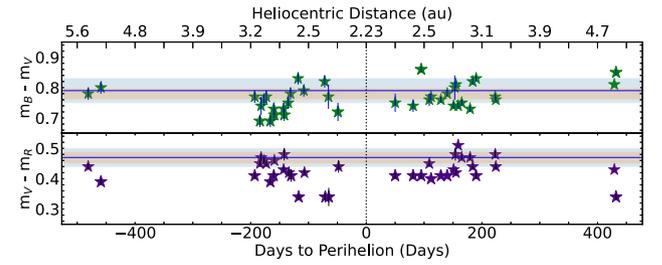
Figure 8. Variation of the colour indices $B - V$ (above) and $V - R$ (below) with DTP and heliocentric distance (in au). The 1σ range for DNCs (Kulyk et al. 2018) is marked as blue and for LPCs (Jewitt 2015) as orange. The blue line is the median value of the DNCs (Kulyk et al. 2018).
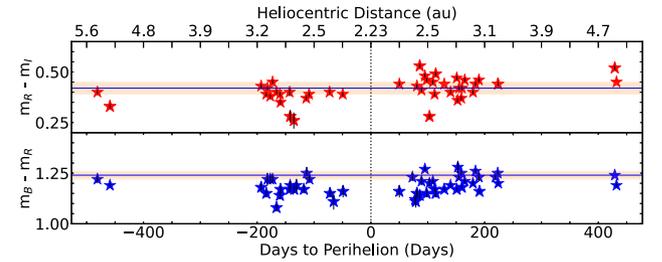
Figure 9. Variation of the colour indices $R - I$ (above) and $B - R$ (below) with DTP and heliocentric distance (in au). The 1σ range for LPCs (Jewitt 2015) is marked as orange. The blue line is the median value of the LPCs (Jewitt 2015).

changed in the apparition, which hints at the homogeneous properties of the dust on the nucleus.

We also checked the contamination by gas contribution in the broad-band colours using our spectroscopic data sets. We used the PYPHOT package (Rodrigo & Solano 2020; Fouesneau 2025) to calculate the magnitude of the flux-calibrated spectrum by first considering the spectrum, which includes the contribution of molecular gas emissions, and second, we used the continuum spectrum of the comet by tracing the dust continuum directly from the observed spectrum. We calculated the magnitude of different filters in both spectra and found that the difference between magnitudes derived from the two spectra is within 0.1, which comes under the error bar of our measurement as mentioned in Table 2. Hence, we are confident

that the computed colours are not significantly affected by the gas emissions.

6.3 Reflective gradient

The reddening of cometary colours gives us a qualitative idea of the size of dust grains present in the cometary comae. A'Hearn et al. (1984) have defined the parameter known as reflective gradient, which is defined as $(dS/d\lambda)/\tilde{S}$, where S is the reflectance of the comet, which is the ratio of the comet flux ($F(\lambda)$) to the solar flux ($F_\odot(\lambda)$), i.e. $S(\lambda) = \frac{F(\lambda)}{F_\odot(\lambda)}$. $d\lambda$ is defined as the difference between two wavelengths, which will be the central bandwidth for different filters, and $\tilde{S}$ is the mean value of the reflectance in the bandpass (Jewitt 2002). Mathematically, it can be written as:

$$S'(\lambda) = \frac{2}{\Delta\lambda} \frac{S(\lambda_2) - S(\lambda_1)}{S(\lambda_2) + S(\lambda_1)} \quad (12)$$

where $\Delta\lambda = \lambda_2 - \lambda_1$, is given in Å. The unit of the reflective gradient, $S'(\lambda)$ is given in per cent $(1000\,\text{Å})^{-1}$. In units of magnitude, we get (Kulyk et al. 2018):

$$S'(\lambda) = \frac{2}{\Delta\lambda} \frac{10^{0.4(CI_{comet} - CI_{sun})} - 1}{10^{0.4(CI_{comet} - CI_{sun})} + 1} \quad (13)$$

Here, CI_{comet} and CI_{sun} are the comet and solar colours. The solar colours have been taken from Holmberg, Flynn & Portinari (2006). Using equation (13), we get the mean value of the normalized spectral gradient for $B - V$ to be 10.90 ± 3.62 per cent $(1000\,\text{Å})^{-1}$, $V - R$ to be 6.15 ± 3.51 per cent $(1000\,\text{Å})^{-1}$, and $R - I$ to be 4.94 ± 3.56 per cent $(1000\,\text{Å})^{-1}$. The trend of decreasing reflectivity with increasing wavelength matches the trend mentioned by Jewitt & Meech (1986), Kulyk et al. (2018), and Shubina et al. (2024).

Kulyk et al. (2018) have provided colour values of 14 comets, including 10 DNCs. Out of these, we have looked at 10 DNCs and found the mean values of the spectral colour gradients for $B - V$ and $V - R$ to be 12 ± 4 and 5 ± 2 per cent $(1000\,\text{Å})^{-1}$, respectively, which are in close agreement to what we have found for comet V2.

6.4 Coma morphology

The surface of a comet is not completely active. There are some active regions that are responsible for the comet's activity. This has been discovered in comets such as 1P/Halley (Reitsema, Delamere & Whipple 1987) and Comet 43P/Wolf–Harrington (Szutowicz 2000). We have studied the coma morphology using the spectra and images of V2 on common dates as discussed in two further sections below.

6.4.1 Measurement of dust activity levels through Afρ

From our spectroscopic observations of 2022 November 22 and December 16, we calculated the dust proxy parameter ($A(0°)f\rho$) using equation (11). Spectra are extracted for apertures in the direction of the east and west sides of the photocentre to check the emission trend. Figs 10(a) and (b) show the variation of $Af\rho$ of the comet in the BC and GC filter passbands on both sides. The positive numbers represent the west side of the comet, and the negative numbers represent the east side of the comet. The significant difference between the two sides is prominent. This shows the asymmetric emissions of the dust. To look for a connection between this asymmetric emission with features in the images, we carried out image processing techniques such as those described by Sekanina & Larson (1984) and Samarasinha, Larson &
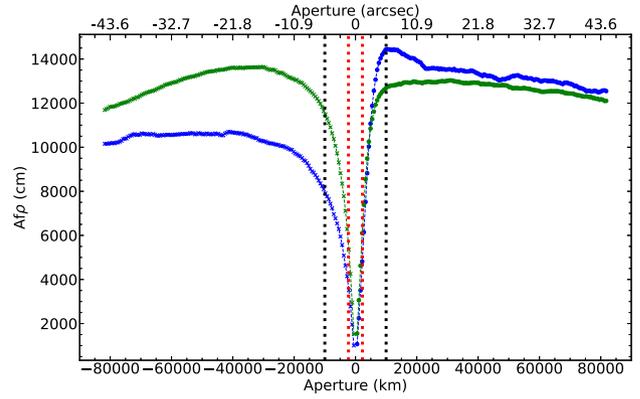
(a) Afρ variation of BC filter in *Blue* and of GC filter in *Green* at the East-side (left) and the West-side (right) on 2022 November 22. The dotted red line shows the Half Width Half Maxima (HWHM), i.e., 1.24 arcsec.
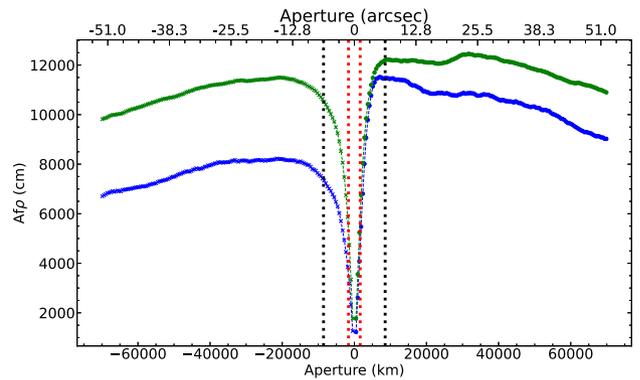

(b) Afρ variation of BC filter in *Blue* and of GC filter in *Green* at the East-side (left) and the West-side (right) on 2022 December 16. The dotted red line shows the Half Width Half Maxima (HWHM), i.e., 1.21 arcsec.

Figure 10. The variation of $Af\rho$ at both sides shows the asymmetry of the emission in the comet. The dotted black line shows the distance at 10 000 km from the photocentre.

Beshore (2006) to reveal the presence of jets or other asymmetric features in the coma.

6.4.2 Investigation of coma structures and asymmetries using image enhancement techniques

For our work, we used the modified version of the Larson–Sekanina (LS) processing technique to extract hidden features. The details are mentioned in Garcia, Gil-Hutton & García-Migani (2020) and Aravind et al. (2022). With this technique, the image is rotated clockwise and counterclockwise at a certain angle, centred on the photocentre, and then subtracted from the original image. After that, the two images are summed to get the final image. We applied this technique to the Bessel B filter images obtained using the HFOSC instrument on 2022 November 22 and December 16. We found two regions with an excess in emission; one is strong, and one is relatively weak, as seen in the two images (Figs 11b and 12b). We have labelled the slit position, which is in the east (left)–west (right) direction. When we compare the images with the spectroscopic results, we see that the $Af\rho$ is following the same trend. We have also applied this technique on the different narrow-band molecular gas filter images obtained using the TRAPPIST telescopes to see similar features on 2022 November 22 (check appendix Figs B1–
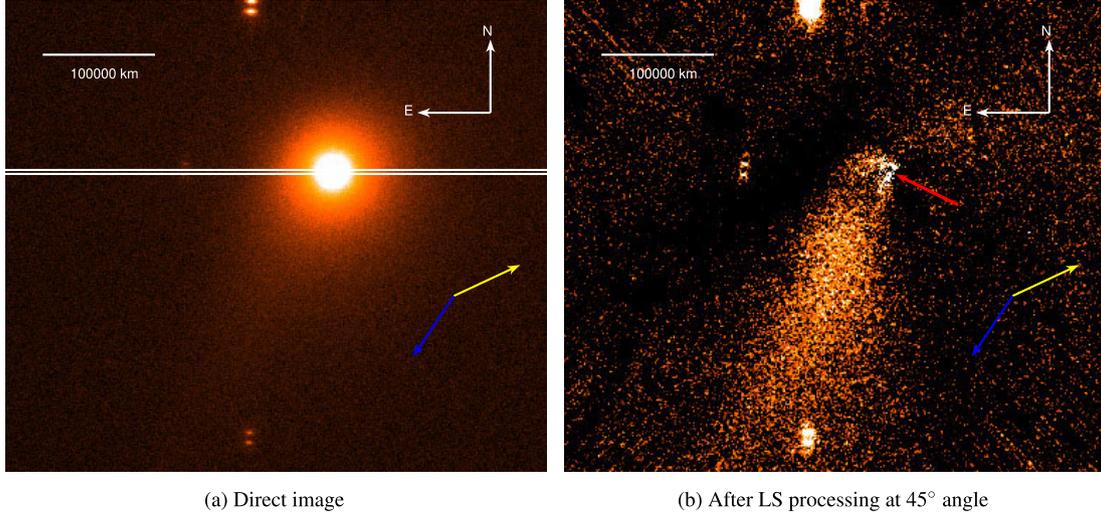
(a) Direct image

(b) After LS processing at 45° angle

Figure 11. *B*-band image observed using HFOSC and HCT on 2022 November 22. The position of the spectrograph slit is in the east–west direction, as shown. The dust-tail orientation and the Sun's direction are marked in blue and yellow. The tail and the projection of the tail (antitail) are visible on either side of the photocentre. The red arrow is pointing towards the photocentre.
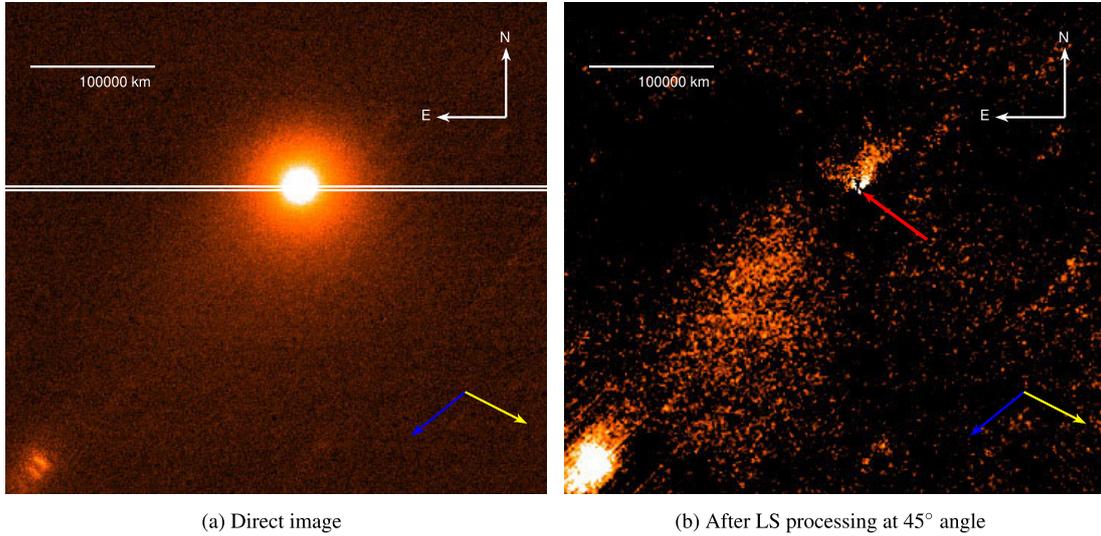
(a) Direct image

(b) After LS processing at 45° angle

Figure 12. *B*-band image observed from HFOSC and HCT on 2022 December 16. The position of the spectrograph slit is in the east–west direction, as shown. The dust-tail orientation and the Sun's direction are marked in blue and yellow. The tail and the projection of the tail (antitail) are visible on either side of the photocentre. The red arrow is pointing towards the photocentre.

B3), and on 2022 December 16 (check appendix Figs B4–B6). We see similar structures in different filters by other image processing techniques, such as applying division by azimuthal median and division by azimuthal average (Samarasinha, Martin & Larson 2013). The strong and weak dust features are consistent with the view of the comet along the orbital plane (orbital plane angle −7.5° and −15.6°, respectively, for the two dates), showing them to coincide with the tail and 'apparent antitail' of the comet.

6.5 Nuclear radius

The nuclear radius of the comet is an important parameter for understanding the size of the minor planetesimals distributed in the Solar system. There are many methods, such as using RADAR (Radio Detection And Ranging) observations (Harmon & Nolan 2005), or using a diffraction-limited imaging telescope. Meech, Hainaut &

Marsden (2004) and Lamy & Toth (1995) have used the *Hubble Space Telescope* to derive the nuclear radius of the comet.

Here, to calculate the size of the comet nucleus, we have used the TRAPPIST photometric observations in the Bessel-*R* filter and used the relation given by Lamy et al. (2004) for calculating the radius of the comet,

$$r_N = \frac{1.496 \times 10^{11}}{\sqrt{p}} \times 10^{0.2 \times [R_\odot - R_N(1,1,0)]} \qquad (14)$$

Here, p is the geometric albedo of the nucleus, which is taken to be 0.04 (Licandro et al. 2016). $R_\odot$ is the apparent magnitude of the Sun in the Bessel-*R* band, i.e. −27.15 (Willmer 2018). $R_N(1, 1, 0)$ is the absolute magnitude of the nucleus, that is, at $r = \Delta = 1$ and phase angle, $\alpha = 0°$. It is given by

$$R_N(1, 1, 0) = R_N - 5\log(r\Delta) + 2.5\log(\phi(\alpha)) \qquad (15)$$

Here, $\phi(\alpha)$ is the phase function corresponding to the phase angle α (Sun–Comet–Observer angle). Since an active coma region can affect the computed radius, it is always better to perform these calculations for comets at large heliocentric distances in order to minimize the coma contribution.

If we start using the details above and assuming that all the light from the comet comes from reflection, we get a radius of around 60–90 km. However, the famous comet C/2014 UN271, whose nuclear radius is around 60 km, was detected around 29 au (Hui et al. 2022). So, if comet V2 was of a similar size, it should have been discovered much earlier than its distance of 8 au at discovery.

Also, it has been known that LPCs are active at even far away distances. Hence, we cannot remove the contribution of the outer coma, which is the reason for the overestimation of the nuclear magnitude and, hence, the nuclear radius. This method by Lamy et al. (2004) is useful when we are sure that there is a minimal coma contribution. However, for an extended body like a comet, it is very difficult to observe them without any significant contribution from the coma. Therefore, we need to estimate the nuclear radius using a different approach.

The method by Sosa & Fernández (2011) uses the non-gravitational parameters to calculate the radius of the comet. The complete force equation of a comet facing non-gravitational forces is:

$$\frac{d^2 \boldsymbol{r}}{dt^2} = -\frac{Gm_\odot \boldsymbol{r}}{r^3} + \nabla \mathcal{R} + A_1 g(r)\hat{\boldsymbol{r}} + A_2 g(r)\hat{\boldsymbol{t}} + A_3 g(r)\hat{\boldsymbol{n}} \quad (16)$$

where G is the gravitational constant, $\mathcal{R}$ is the planetary disturbing function, $M_\odot$ is the Sun's mass, r is the heliocentric distance, and $g(r)$ is the empirical function of the H_2O or CO sublimation rate, which is given by:

$$g(r) = \alpha \left(\frac{r}{r_0}\right)^{-m} \left[1 + \left(\frac{r}{r_0}\right)^n\right]^{-k} \quad (17)$$

The different values of parameters such as α, m, n, k, and r_0 depend on whether the water or CO is sublimating. Using the details mentioned in Królikowska & Dybczyński (2017), the above parameters depend on the value of perihelion. Since the perihelion of comet V2 is less than 4 au, the $g(r)$ function represents the water sublimation, and hence the parametric values are $\alpha = 0.1113$, $m = 2.15$, $n = 5.093$, $k = 4.6142$, and $r_0 = 2.808$ au.

In the non-gravitational models, the A_1, A_2, and A_3 represent the modulus of the non-gravitational acceleration in the radial, transverse, and normal directions at 1 au from the Sun. There are two models: the symmetric and asymmetric models. In the symmetric model, only two parameters (A_1 and A_2) are used to estimate the non-gravitational acceleration, J:

$$J = \sqrt{A_1^2 + A_2^2} \times g[r(t)] \quad (18)$$

while, for the asymmetric model, two more parameters, A_3 and DT, where DT is the time offset of maximum brightness, are involved:

$$J = \sqrt{A_1^2 + A_2^2 + A_3^2} \times g[r(t - DT)] \quad (19)$$

Since the comet's emission looks asymmetric in Figs 10(a) and (b), we will use the asymmetric method. Here, we consider a comet of mass M_N, which is dominated by water molecules, and $Q(r)$, which is the production rate of water H_2O. At 3 au, we are at the limit where water sublimation starts to decay. Since we have observed $Q(OH)$ from TRAPPIST, using the relation mentioned in Lamy et al. (2009), i.e. $Q(H_2O) = 1.1 \times Q(OH)$, we get the production rate of water, $Q(H_2O)$. We then used equation (3) given in Sosa & Fernández

(2011),

$$M_N J = Q m u \quad (20)$$

where J is the non-gravitational acceleration, m is the mass of a dominant sublimating molecule, i.e. water (H_2O), and u is the effective outflow velocity, which is taken to be 0.27 km s^{-1} (Sosa & Fernández 2011). The mass of the comet is then defined as,

$$M_N = \frac{Q m u}{J} = \frac{Q m u}{A g} \quad (21)$$

Here, A is $\sqrt{A_1^2 + A_2^2 + A_3^2}$, and, for comet V2, $A_1 = (5.85 \pm 0.01) \times 10^{-8}$ au d^{-2}, $A_2 = (5 \pm 2) \times 10^{-9}$ au d^{-2}, $A_3 = (-6.0 \pm 0.3) \times 10^{-9}$ au d^{-2}, and $DT = (-179 \pm 9)$ d-, from NASA's JPL website. After calculating it, we get the median mass to be $(3.4 \pm 0.8) \times 10^{12}$ kg. Here, the error in mass is calculated using the error propagation of all the variables as shown in equation (22):

$$\delta M = M \times ((\delta Q/Q)^2 + (\delta J/J)^2) \quad (22)$$

where, δJ would be calculated as:

$$\delta J = J \times \sqrt{\begin{array}{l} \frac{A_1^2}{A_1^2 + A_2^2 + A_3^2} \times \delta A_1^2 + \frac{A_2^2}{A_1^2 + A_2^2 + A_3^2} \times \delta A_2^2 \\ + \frac{A_3^2}{A_1^2 + A_2^2 + A_3^2} \times \delta A_3^2 \end{array}} \quad (23)$$

Now, considering the bulk density $\rho = 537.8 \pm 0.6$ kg m^{-3} which has been derived (Pätzold et al. 2018) using RSI experiment onboard *Rosetta* mission, the radius of the comet is computed as:

$$R_N = \left(\frac{3M_N}{4\pi\rho}\right)^{1/3} \quad (24)$$

Using the above equation, we get the radius of the cometary nucleus to be 1.1 ± 0.1 km.

7 CONCLUSIONS

We have observed comet C/2020 V2 using multiple telescopes in imaging and spectroscopic mode. The observations span 32 months across perihelion. From these observations, we conclude the following:

(i) The gas production rate ratios, such as C_2/CN and C_3/CN, indicate that the comet has a typical carbon composition.

(ii) The dust-to-gas ratio shows that the comet has a dust-rich composition.

(iii) The small variations in production rate ratios and the gas-to-dust ratios over the long-term observations show that the nucleus of the comet is homogeneous.

(iv) The mean colours, such as $B - V = 0.77 \pm 0.04$, $V - R = 0.43 \pm 0.04$, $R - I = 0.42 \pm 0.06$, and $B - R = 1.19 \pm 0.04$, are similar to the median values found for LPCs ($B - V = 0.78 \pm 0.02$, $V - R = 0.47 \pm 0.02$, $R - I = 0.42 \pm 0.03$, and $B - R = 1.24 \pm 0.02$) and median value of DNCs ($B - V = 0.80 \pm 0.07$, and $V - I = 0.44 \pm 0.07$). Departures from the average colours with respect to the heliocentric distance could be due to changes in the activity of the comet. However, the averages of the pre- and post-perihelion colours of comet V2 are quite similar. Moreover, the effect of gas contamination in broad-band colours is found to be negligible in this comet.

(v) The mean value of the reflectivity gradient is found to be 10.9 ± 3.6 per cent/1000 Å for $B - V$, 6.2 ± 3.5 per cent/1000 Å

for $V - R$, which is similar to the other DNCs. For $R - I$, the value is found to be 4.9 ± 3.6 per cent/1000 Å.

(vi) Spectroscopic calculation of $Af\rho$ shows asymmetry on either side of the photocentre. LS processing technique on the images of the same dates shows excess emission regions, where one is along the comet's dust tail, while the other is along the antitail.

(vii) The non-gravitational force model provides an estimate of the comet's nuclear radius to be 1.1 ± 0.1 km.

(viii) The compositionally homogenous nature of comet V2 indicates that the formation location of this comet in the early Solar system was homogeneously mixed. However, this is an indirect inference and is open to interpretation.

This work shows that DNCs that exhibit steady behaviour in their early orbital evolution may continue with a similar stable nature throughout their orbit. This is an important input for the *Comet Interceptor* mission, to select a suitable DNC early enough in its orbital path, allowing for more time to plan the encounter. It also emphasizes the requirement to closely monitor newly discovered comets photometrically alongside the usually carried out astrometric observations to determine their orbital characteristics. Periodic spectroscopic observations would help confirm the narrow-band photometric measurements and also help to fully understand the cometary composition.

ACKNOWLEDGEMENTS

CONFLICT OF INTEREST

The authors declare that there are no conflicts of interest regarding this work.

DATA AVAILABILITY

The data underlying this article will be shared on reasonable request to the corresponding author.

REFERENCES

A'Hearn M. F., Millis R. C., Schleicher D. G., Osip D. J., Birch P. V., 1995, Icarus, 118, 223

A'Hearn M. F., Schleicher D. G., Millis R. L., Feldman P. D., Thompson D. T., 1984, AJ, 89, 579

Aravind K., Ganesh S., Venkataramani K., Sahu D., Angchuk D., Sivarani T., Unni A., 2021, MNRAS, 502, 3491

Aravind K., Halder P., Ganesh S., Sahu D., Serra-Ricart M., Chambó J. J., Angchuk D., Sivarani T., 2022, Icarus, 383, 115042

Aravind K., Venkataramani K., Ganesh S., Jehin E., Moulane Y., 2024, J. Astrophys. Astron., 45, 11

Astropy Collaboration, 2013, A&A, 558, A33

Barkaoui K., Gillon M., Benkhaldoun Z., Emmanuel J., Elhalkouj T., Daassou A., Burdanov A., Delrez L., 2017, J. Phys.: Conf. Ser., 869, 012073

Barnes J., Hayes D., Observatory K. P. N., 1984, IRS Standard Star Manual. Association of Universities for Research in Astronomy, https://books.google.co.in/books?id = kJzvAAAAMAAJ

Brasser R., Morbidelli A., 2013, Icarus, 225, 40

Brasser R., Wang J. H., 2015, A&A, 573, A102

Cannon A. J., Pickering E. C., 1918, Ann. Harvard Coll. Obs., 91, 1

Duncan M. J., Levison H. F., 1997, Science, 276, 1670

Dybczyński P. A., Królikowska M., 2011, MNRAS, 416, 51

Farnham T. L., Schleicher D. G., A'Hearn M. F., 2000, Icarus, 147, 180

Filippenko A. V., 1982, PASP, 94, 715

Fink Uwe, Hicks M. D., 1996, ApJ, 459, 729

Fouesneau M., 2025, pyphot. Zenodo, https://doi.org/10.5281/zenodo.14712174

Garcia R., Gil-Hutton R., García-Migani E., 2020, Planet. Space Sci., 180, 104779

Gomes R., Levison H. F., Tsiganis K., Morbidelli A., 2005, Nature, 435, 466

Harmon J. K., Nolan M. C., 2005, Icarus, 176, 175

Haser L., 1957, Bull. Soc. R. Sci. Liege, 43, 740

Holmberg J., Flynn C., Portinari L., 2006, MNRAS, 367, 449

Hui M.-T., Jewitt D., Yu L.-L., Mutchler M. J., 2022, ApJ, 929, L12

Ivanova O., Luk'yanyk I., Tomko D., Moiseev A., 2021, MNRAS, 507, 5376

Jehin E. et al., 2011, The Messenger, 145, 2

Jewitt D. C., 2002, AJ, 123, 1039

Jewitt D., 2015, AJ, 150, 201

Jewitt D., Meech K. J., 1986, ApJ, 310, 937

Jones G. H. et al., 2024, Space Sci. Rev., 220, 9

Królikowska M. g., Dybczyński P. A., 2010, MNRAS, 404, 1886

Królikowska M. g., Dybczyński P. A., 2017, MNRAS, 472, 4634

Królikowska M., 2014, A&A, 567, A126

Kulyk I., Rousselot P., Korsun P. P., Afanasiev V. L., Sergeev A. V., Velichko S. F., 2018, A&A, 611, A32

Lamy P. L., Toth I., 1995, A&A, 293, L43

Lamy P. L., Toth I., Fernandez Y. R., Weaver H. A., 2004, in Festou M. C., Keller H. U., Weaver H. A. eds, Comets II, p. 223

Lamy P. L., Toth I., Weaver H. A., A'Hearn M. F., Jorda L., 2009, A&A, 508, 1045

Landolt A. U., 1992, AJ, 104, 340

Langland-Shula L. E., Smith G. H., 2011, Icarus, 213, 280

Lee S., Park S.-J., 2006, J. Korean Astron. Soc., 39, 151

Levison H. F., 1992, in Harris A. W., Bowell E. eds, Asteroids, Comets, Meteors 1991, p. 353

Levison H. F., 1996, in Rettig T. W., Hahn J. M., eds, ASP Conf. Ser. Vol. 107, Completing the Inventory of the Solar System, p. 173

Levison H. F., Duncan M. J., 1997, Icarus, 127, 13

Levison H. F., Duncan M. J., Dones L., Gladman B. J., 2006, Icarus, 184, 619

Licandro J., Alí-Lagoa V., Tancredi G., Fernández Y., 2016, A&A, 585, A9

Meech K., Hainaut O., Marsden B., 2004, Icarus, 170, 463

Morbidelli A., Tsiganis K., Crida A., Levison H. F., Gomes R., 2007, AJ, 134, 1790

Mousavi S. J., Farsani M. H., Darbani S. M. R., Asadorian N., Soltanolkotabi M., Majd A. E., 2015, Appl. Opt., 54, 1713

Nesvorný D., Vokrouhlický D., Dones L., Levison H. F., Kaib N., Morbidelli A., 2017, ApJ, 845, 27

Oke J. B., 1990, AJ, 99, 1621

Oort J. H., 1950, Bull. Astron. Inst. Netherlands, 11, 91

Opitom C., Jehin E., Manfroid J., Hutsemékers D., Gillon M., Magain P., 2015, A&A, 584, A121

Pätzold M. et al., 2018, MNRAS, 483, 2337

Portnov A., Rosenwaks S., Bar I., 2003, Appl. Opt., 42, 2835

Prabhu T. P., 2014, Proc. Indian Natl. Sci. Acad. A, 80, 887

Reitsema H. J., Delamere W. A., Whipple F. L., 1987, in Rolfe E. J., Battrick B., Ackerman M., Scherer M., Reinhard R.eds, ESA SP-278, Diversity and Similarity of Comets, p. 455

Rodrigo C., Solano E., 2020, XIV.0 Scientific Meeting (virtual) of the Spanish Astronomical Society, p. 182

Samarasinha N. H., Larson S., Beshore E., 2006, AAS/Division for Planetary Sciences Meeting Abstracts #38, p. 29.13

Samarasinha N. H., Martin M. P., Larson S. M., 2013, Cometary Coma Image Enhancement Facility, http://cie.psi.edu

Schleicher D. G., 2007, Icarus, 191, 322

Schleicher D. G., 2010, AJ, 140, 973

Schleicher D. G., Millis R. L., Birch P. V., 1998, Icarus, 132, 397

Sekanina Z., Larson S. M., 1984, AJ, 89, 1408

Shubina O., Ivanova O., Petrov D., Luk'yanyk I., Rosenbush V., Kiselev N., 2024, MNRAS, 528, 7027

Sosa A., Fernández J. A., 2011, MNRAS, 416, 767

Stalin C. S., Hegde M., Sahu D. K., Parihar P. S., Anupama G. C., Bhatt B. C., Prabhu T. P., 2008, Bull. Astron. Soc. India, 36, 111

Stone R. C., 1996, PASP, 108, 1051

Swings P., 1941, Lick Obs. Bull., 19, 131

Szutowicz S., 2000, A&A, 363, 323

Tsiganis K., Gomes R., Morbidelli A., Levison H. F., 2005, Nature, 435, 459

Van Dokkum P. G., 2001, PASP, 113, 1420

Venkataramani K., Ghetiya S., Ganesh S., Joshi U. C., Agnihotri V. K., Baliyan K. S., 2016, MNRAS, 463, 2137

Voitko A., Ivanova O., 2024, in European Planetary Science Congress, p. EPSC2024–460

Walsh K. J., Morbidelli A., Raymond S. N., O'Brien D. P., Mandell A. M., 2011, Nature, 475, 206

Wang J. H., Brasser R., 2014, A&A, 563, A122

Willmer C. N. A., 2018, ApJS, 236, 47

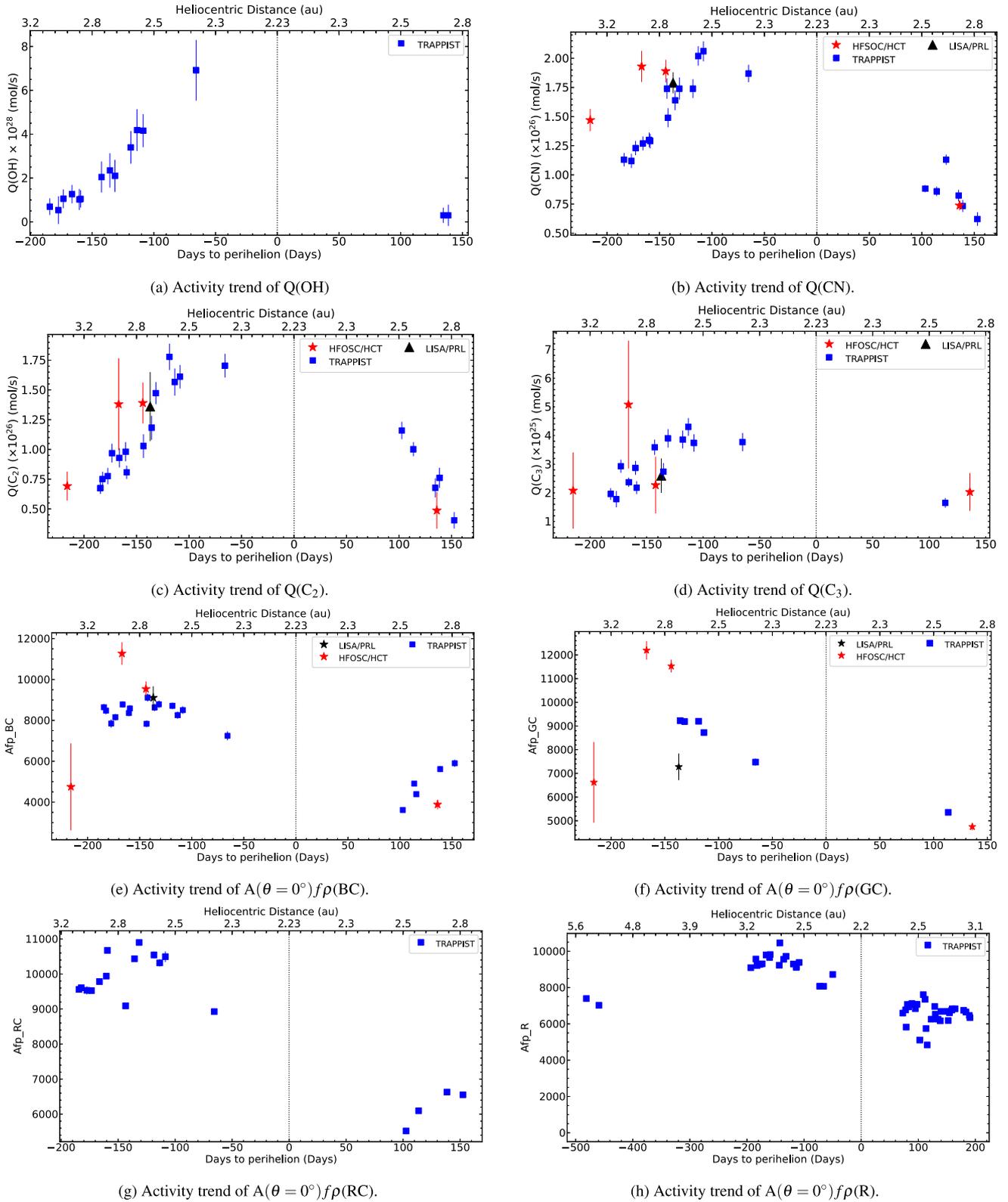## APPENDIX A: VARIATION OF GAS PRODUCTION RATES AND DUST PROXY PARAMETER $Af\rho$ IN COMET C/2020 V2

(a) Activity trend of Q(OH)

(b) Activity trend of Q(CN).

(c) Activity trend of Q(C$_2$).

(d) Activity trend of Q(C$_3$).

(e) Activity trend of A($\theta = 0°$)$f\rho$(BC).

(f) Activity trend of A($\theta = 0°$)$f\rho$(GC).

(g) Activity trend of A($\theta = 0°$)$f\rho$(RC).

(h) Activity trend of A($\theta = 0°$)$f\rho$(R).

Figure A1. Activity trends of comet C/2020 V2 as a function of DTP and heliocentric distance (au).

APPENDIX B: LS PROCESSING ON TRAPPIST NARROW-BAND IMAGES

Here, we present the TRAPPIST narrow-band filter images of CN, C_2, and C_3 molecules observed on 2022 November 22 and December 16 [(Figs B1a, B2a, and B3a) and (Figs B4a, B5a, and B6a)], along with the corresponding LS processing on these images [(Figs B1b, B2b, and B3b) and (Figs B4b, B5b, and B6b)], using the details mentioned in Section 6.4.
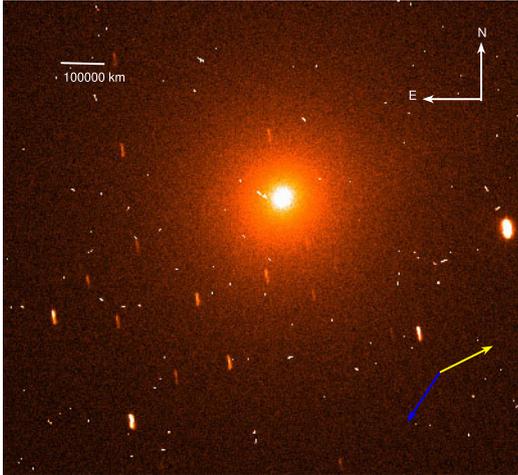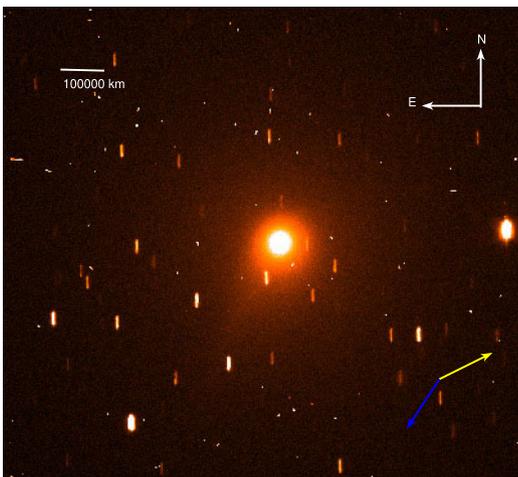

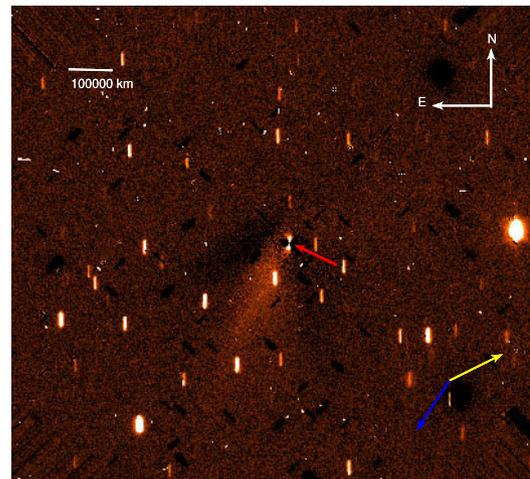(a) TRAPPIST CN filter image observed on 2022 November 22
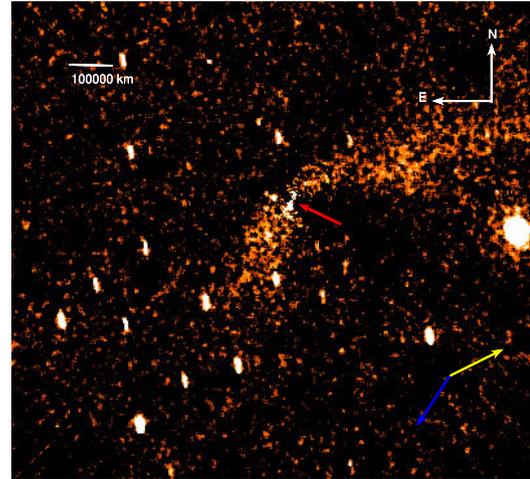
(b) LS processing on the CN image observed on 2022 November 22

Figure B1. Image of CN filter and its corresponding LS processed. The dust-tail orientation and the Sun's direction are marked in blue and yellow. The red arrow is pointing towards the photocentre.

(a) TRAPPIST C_2 filter image observed on 2022 November 22

(b) LS processing on the C_2 image observed on 2022 November 22

Figure B2. Image of C_2 filter and its corresponding LS processed. The dust-tail orientation and the Sun's direction are marked in blue and yellow. The red arrow is pointing towards the photocentre.
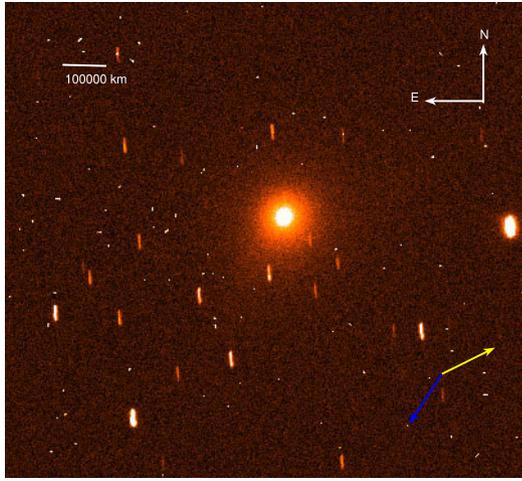
(a) TRAPPIST C_3 filter image observed on 2022 November 22

(b) LS processing on the C_3 image observed on 2022 November 22

Figure B3. Image of C_3 filter and its corresponding LS processed. The dust-tail orientation and the Sun's direction are marked in blue and yellow. The red arrow is pointing towards the photocentre.
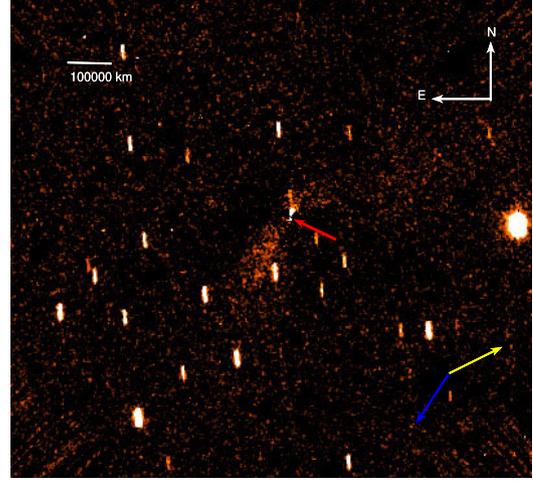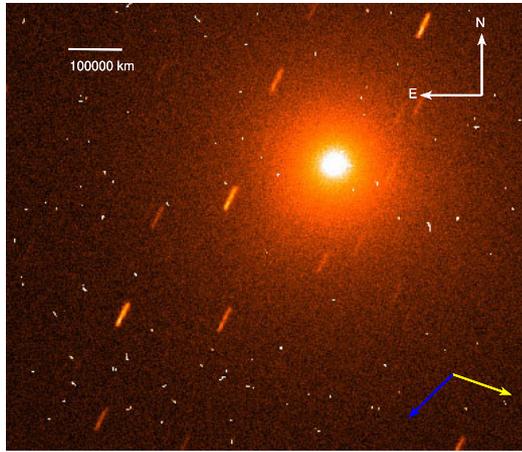

(a) TRAPPIST CN filter image observed on 2022 December 16

(b) LS processing on the CN image observed on 2022 December 16

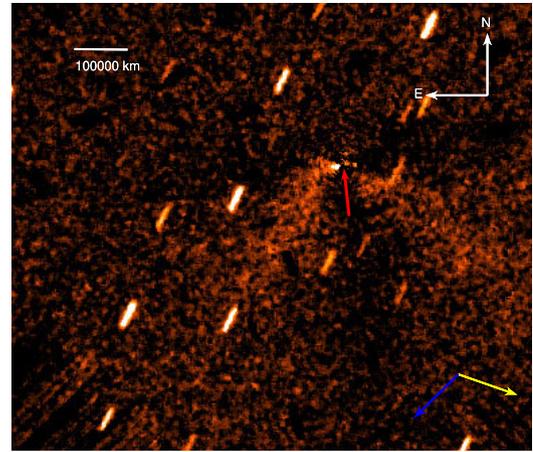**Figure B4.** Image of CN filter and its corresponding LS processed. The dust-tail orientation and the Sun's direction are marked in blue and yellow. The red arrow is pointing towards the photocentre.

(a) TRAPPIST C_2 filter image observed on 2022 December 16

(b) LS processing on the C_2 image observed on 2022 December 16

Figure B5. Image of C_2 filter and its corresponding LS processed. The dust-tail orientation and the Sun's direction are marked in blue and yellow. The red arrow is pointing towards the photocentre.
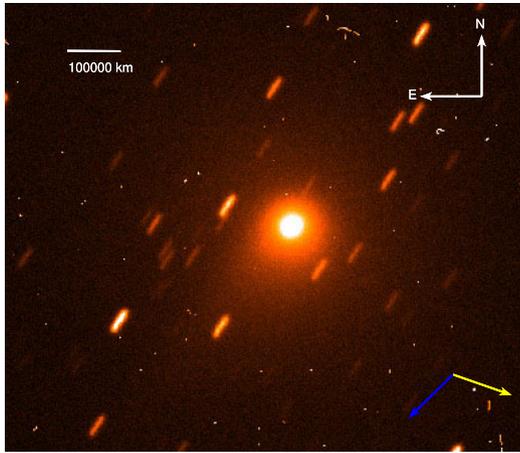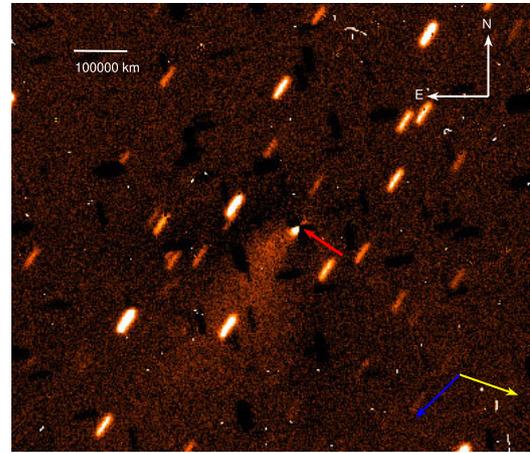

(a) TRAPPIST C_3 filter image observed on 2022 December 16

(b) LS processing on the C_3 image observed on 2022 December 16

Figure B6. Image of C_3 filter and its corresponding LS processed. The dust-tail orientation and the Sun's direction are marked in blue and yellow. The red arrow is pointing towards the photocentre.
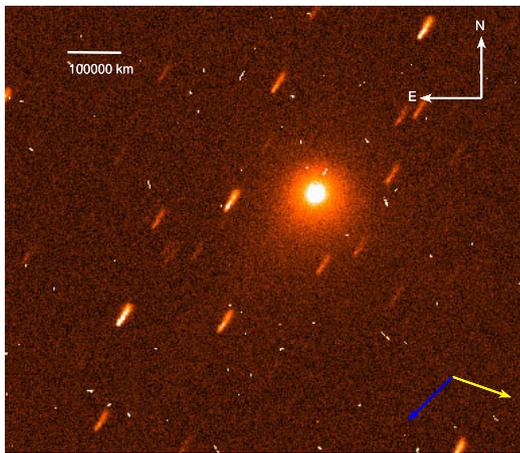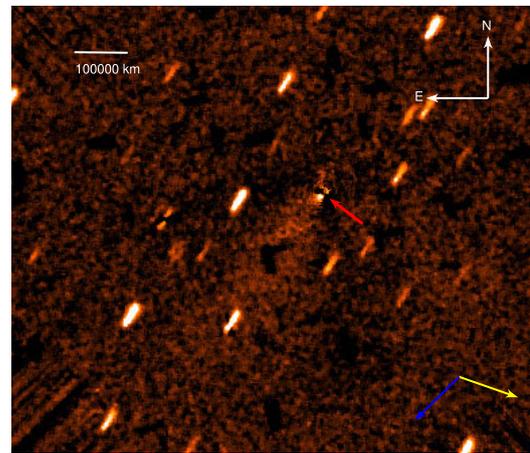
APPENDIX C: TRAPPIST MAGNITUDES IN DIFFERENT FILTERS AND $A f \rho$ IN BROAD-BAND R FILTER

Table C1. TRAPPIST magnitudes of comet V2 with different broad-band filters, *B*, *V*, *R*, and *I*, and the $Af\rho$ in broad-band *R* filter observed from both TN and TS telescopes.

Date	DTP (d)	r (au)	Δ (au)	Telescope TN/TS	B	V	R	I	$A(\theta=0°)f\rho$ (cm) R
2022 Jan 11	−481.28	−5.41	5.00	TN	16.27 ± 0.02	15.49 ± 0.01	15.05 ± 0.01	14.65 ± 0.01	7395 ± 42
2022 Feb 02	−459.33	−5.23	4.62	TN	16.08 ± 0.01	15.28 ± 0.01	14.89 ± 0.01	14.56 ± 0.01	7023 ± 37
2022 Oct 26	−193.34	−3.10	3.10	TN	14.48 ± 0.02	13.70 ± 0.01	13.29 ± 0.01	12.86 ± 0.01	9097 ± 75
2022 Nov 04	−184.37	−3.04	2.91	TN	14.27 ± 0.02	13.58 ± 0.01	13.13 ± 0.01	12.74 ± 0.01	9572 ± 71
2022 Nov 06	−182.36	−3.02	2.86	TN	14.34 ± 0.02	13.59 ± 0.01	13.12 ± 0.01	12.70 ± 0.01	9216 ± 72
2022 Nov 11	−177.38	−2.98	2.76	TN	14.27 ± 0.02	13.51 ± 0.01	13.05 ± 0.01	12.67 ± 0.01	9275 ± 96
2022 Nov 15	−173.38	−2.96	2.67	TN	14.23 ± 0.02	13.46 ± 0.01	13.01 ± 0.01	12.56 ± 0.01	9307 ± 70
2022 Nov 22	−166.39	−2.91	2.53	TN	13.95 ± 0.02	13.26 ± 0.01	12.87 ± 0.01	12.48 ± 0.01	9796 ± 72
2022 Nov 28	−160.40	−2.87	2.42	TN	13.95 ± 0.02	13.22 ± 0.01	12.81 ± 0.01	12.42 ± 0.01	9655 ± 70
2022 Nov 29	−159.41	−2.86	2.41	TN	13.93 ± 0.02	13.22 ± 0.01	12.76 ± 0.01	12.42 ± 0.01	9819 ± 71
2022 Dec 15	−143.45	−2.76	2.18	TN	13.79 ± 0.02	13.06 ± 0.01	12.63 ± 0.01	12.23 ± 0.02	9231 ± 83
2022 Dec 16	−142.42	−2.75	2.17	TN	13.68 ± 0.02	12.97 ± 0.01	12.49 ± 0.01	12.21 ± 0.03	10462 ± 126
2022 Dec 23	−135.67	−2.71	2.11	TN	13.65 ± 0.02	12.90 ± 0.01	12.48 ± 0.01	12.22 ± 0.04	9561 ± 94
2022 Dec 27	−131.61	−2.68	2.08	TN	13.65 ± 0.02	12.87 ± 0.01	12.46 ± 0.01	–	9723 ± 234
2023 Jan 09	−118.68	−2.60	2.07	TN	13.64 ± 0.02	12.81 ± 0.01	12.47 ± 0.01	–	9298 ± 86
2023 Jan 14	−113.55	−2.58	2.08	TN	13.74 ± 0.02	–	12.48 ± 0.01	12.11 ± 0.01	9110 ± 123
2023 Jan 19	−108.56	−2.55	2.11	TN	13.64 ± 0.02	12.85 ± 0.01	12.43 ± 0.01	12.04 ± 0.01	9386 ± 100
2023 Feb 24	−72.69	−2.38	2.55	TN	13.85 ± 0.02	13.03 ± 0.01	12.69 ± 0.01	12.29 ± 0.01	8074 ± 65
2023 Mar 03	−65.65	−2.35	2.65	TN	13.83 ± 0.03	13.06 ± 0.02	12.73 ± 0.02	–	8070 ± 110
2023 Mar 19	−49.71	−2.30	2.87	TN	13.70 ± 0.03	12.98 ± 0.01	12.54 ± 0.01	12.15 ± 0.01	8722 ± 94
2023 June 26	49.91	2.30	2.88	TS	14.04 ± 0.03	13.29 ± 0.01	12.88 ± 0.01	12.44 ± 0.01	–
2023 July 19	72.88	2.38	2.55	TS	14.18 ± 0.02	–	12.95 ± 0.01	–	6592 ± 55
2023 July 24	77.84	2.40	2.47	TS	14.10 ± 0.02	–	12.98 ± 0.01	–	6769 ± 63
2023 July 25	78.83	2.40	2.45	TS	14.15 ± 0.02	–	13.05 ± 0.01	–	5822 ± 56
2023 July 27	80.86	2.41	2.42	TS	14.02 ± 0.02	13.28 ± 0.01	12.87 ± 0.01	12.44 ± 0.01	7068 ± 53
2023 July 29	83.00	2.42	2.40	TS	–	–	12.89 ± 0.01	–	6937 ± 53
2023 Aug 01	85.85	2.44	2.34	TS	14.01 ± 0.02	–	12.87 ± 0.01	12.35 ± 0.01	7061 ± 59
2023 Aug 04	88.89	2.45	2.29	TS	14.01 ± 0.02	–	12.80 ± 0.01	12.38 ± 0.01	7124 ± 54
2023 Aug 10	94.87	2.48	2.19	TS	14.09 ± 0.02	13.23 ± 0.01	12.82 ± 0.01	12.34 ± 0.01	6837 ± 42
2023 Aug 13	97.85	2.49	2.15	TS	13.94 ± 0.02	12.77 ± 0.01	12.79 ± 0.01	12.33 ± 0.01	7075 ± 66
2023 Aug 16	101.00	2.51	2.10	TS	–	13.25 ± 0.01	–	12.38 ± 0.01	–
2023 Aug 18	102.64	2.52	2.08	TN	14.25 ± 0.02	–	13.05 ± 0.01	12.77 ± 0.01	5108 ± 34
2023 Aug 24	108.76	2.55	2.00	TS	13.82 ± 0.02	13.06 ± 0.01	12.61 ± 0.01	12.16 ± 0.01	7609 ± 54
2023 Aug 27	111.90	2.57	1.97	TS	13.79 ± 0.01	13.02 ± 0.01	12.62 ± 0.01	12.23 ± 0.01	7352 ± 42
2023 Aug 29	113.60	2.58	1.95	TN	14.05 ± 0.02	–	12.90 ± 0.01	12.41 ± 0.01	5744 ± 46
2023 Aug 31	116.00	2.59	1.93	TS	–	–	13.04 ± 0.01	–	4840 ± 60
2023 Sept 07	123.00	2.63	1.88	TS	–	–	12.53 ± 0.01	–	6258 ± 55
2023 Sept 13	128.83	2.66	1.86	TS	13.72 ± 0.01	12.96 ± 0.01	12.55 ± 0.01	12.11 ± 0.01	6960 ± 34
2023 Sept 23	138.49	2.72	1.87	TS	–	–	12.71 ± 0.01	–	6169 ± 72
2023 Sept 24	139.72	2.73	1.87	TS	13.73 ± 0.01	12.95 ± 0.01	12.54 ± 0.01	12.14 ± 0.01	6684 ± 34
2023 Oct 05	150.64	2.80	1.96	TS	13.86 ± 0.01	13.12 ± 0.01	12.69 ± 0.01	12.22 ± 0.01	6686 ± 42
2023 Oct 07	152.48	2.81	1.99	TN	14.03 ± 0.03	13.23 ± 0.02	12.75 ± 0.01	12.40 ± 0.01	6182 ± 34
2023 Oct 09	154.72	2.83	2.01	TS	13.97 ± 0.01	13.16 ± 0.01	12.74 ± 0.01	12.32 ± 0.01	6614 ± 48
2023 Oct 13	158.73	2.86	2.07	TS	14.02 ± 0.01	13.28 ± 0.01	12.77 ± 0.01	12.40 ± 0.01	6762 ± 37
2023 Oct 14	159.65	2.86	2.09	TS	14.03 ± 0.01	–	12.85 ± 0.01	12.43 ± 0.01	6832 ± 34
2023 Oct 19	164.53	2.90	2.17	TS	14.15 ± 0.02	13.40 ± 0.01	12.93 ± 0.01	12.48 ± 0.01	6831 ± 39
2023 Nov 03	179.49	3.00	2.47	TS	14.44 ± 0.02	13.71 ± 0.01	13.24 ± 0.01	12.84 ± 0.01	6749 ± 40
2023 Nov 07	183.57	3.03	2.56	TS	14.59 ± 0.01	13.78 ± 0.01	13.34 ± 0.01	12.90 ± 0.00	6653 ± 33
2023 Nov 13	189.50	3.07	2.70	TS	14.70 ± 0.01	13.88 ± 0.01	13.47 ± 0.01	13.01 ± 0.00	6464 ± 65
2023 Nov 14	190.58	3.08	2.73	TS	14.69 ± 0.01	–	13.53 ± 0.01	–	6342 ± 35
2023 Dec 05	212.00	3.24	3.24	TS	15.03 ± 0.01	–	–	–	–
2023 Dec 12	219.00	3.29	3.41	TS	15.13 ± 0.01	–	13.90 ± 0.01	–	–
2023 Dec 13	220.00	3.30	3.43	TS	–	–	13.87 ± 0.01	–	–
2023 Dec 16	223.00	3.32	3.50	TS	15.18 ± 0.01	14.41 ± 0.01	13.93 ± 0.01	13.49 ± 0.01	–
2023 Dec 17	224.00	3.33	3.52	TS	15.18 ± 0.01	14.42 ± 0.01	13.98 ± 0.01	13.54 ± 0.01	–
2024 July 09	429.00	4.98	4.47	TS	16.53 ± 0.01	15.72 ± 0.01	15.29 ± 0.01	14.77 ± 0.01	–
13-07-2024 July 13	432.00	5.00	4.47	TS	16.52 ± 0.01	15.67 ± 0.01	15.33 ± 0.01	14.88 ± 0.01	–
2024 Aug 13	463.00	5.26	4.47	TS	–	–	15.37 ± 0.01	–	–

This paper has been typeset from a TEX/LATEX file prepared by the author.